Detyrosination enrichment on microtubule subsets is established by the interplay between a stochastically-acting enzyme and microtubule stability

Qing Tang[1], Sebastian Sensale[2,3, †, *], Charles Bond[1, †], Andy Qiao[2], Siewert Hugelier[1], Arian Arab[1], Gaurav Arya[2], Melike Lakadamyali[1, *]

[1]Department of Physiology, Perelman School of Medicine, University of Pennsylvania, Philadelphia, PA 19104

[2]Department of Mechanical Engineering and Materials Science, Duke University, Durham, NC 27708, USA

[3]Department of Physics, Cleveland State University, Cleveland, OH 44115-2214, USA

[†] equal contribution

* Correspondence should be sent to M.L.: melikel@pennmedicine.upenn.edu and S.S.: s.sensalerodriguez@csuohio.edu

Abstract

Microtubules in cells consist of functionally diverse subpopulations carrying distinct post-translational modifications (PTMs). Akin to the histone code, the tubulin code regulates a myriad of microtubule functions ranging from intracellular transport to chromosome segregation. Yet, how individual PTMs only occur on subsets of microtubules to contribute to microtubule specialization is not well understood. In particular, microtubule detyrosination, which is the removal of the C-terminal tyrosine on α-tubulin subunits, marks the stable population of microtubules and modifies how microtubules interact with other microtubule-associated proteins to regulate a wide range of cellular processes. Previously, we found that, in certain cell types, only a small subpopulation of microtubules is highly enriched with the detyrosination mark (~30%) and that detyrosination spans most of the length of a microtubule, often adjacent to a completely tyrosinated microtubule. How the activity of a cytosolic detyrosinase, Vasohibin (VASH) leads to only a small subpopulation of highly detyrosinated microtubules is unclear. Here, using quantitative super-resolution microscopy, we visualized nascent microtubule detyrosination events in cells consisting of 1-3 detyrosinated α-tubulin subunits after Nocodazole washout. Microtubule detyrosination accumulates slowly and in a disperse pattern across the microtubule length. By visualizing single molecules of VASH in live cells, we found that VASH engages with microtubules stochastically on a short time scale suggesting limited removal of tyrosine per interaction, consistent with the super-resolution results. Combining these quantitative imaging results with simulations incorporating

parameters from our experiments, we propose a stochastic model for cells to establish a subset of detyrosinated microtubules via a detyrosination-stabilization feedback mechanism.

Introduction

Microtubules experience numerous posttranslational modifications (PTMs), including polyglutamylation, acetylation and detyrosination, which segregate them into distinct subpopulations with diverse mechanical and functional properties (Janke and Magiera, 2020; Roll-Mecak, 2019). Little is known about how certain microtubule PTMs are present or enriched on only subsets of the total microtubule population. Microtubules are dynamic cylindrical polymers assembled from α, β-tubulin heterodimers, the C-terminal tails of which are exposed to the cytosol and are particularly enriched with PTMs. These cytosolic tubulin tail modifications allow direct tuning of interactions between microtubules and many microtubule-associated proteins (MAPs). Most α-tubulin isoforms encode a C-terminal tyrosine, which can be removed by the recently discovered carboxypeptidase Vasohibin (VASH) (Aillaud et al., 2017; Nieuwenhuis et al., 2017) and another newly discovered tyrosine carboxylpeptidase MATCAP (Landskron et al., 2022). It has been shown that both in the mouse brain and in vitro cell lines, VASH is the major detyrosinase that accounts for the vast majority of detyrosination (~ 75% in mouse brain (Aillaud et al., 2017)), whereas MATCAP only contributes a modest amount of detyrosination (Landskron et al., 2022; Nieuwenhuis et al., 2017). Detyrosination changes how certain MAPs interact with the C-terminal tail of α-tubulins on microtubules, including those containing the cytoskeleton-associated protein glycine-rich (CAP-Gly) domain that directly recognizes the tyrosine residue of the EEY/F motif at the C terminus of α-tubulin and preferentially binds to tyrosinated tubulin (Bieling et al., 2008; Chen et al., 2021; McKenney et al., 2016; Peris et al., 2006; Steinmetz and Akhmanova, 2008; Weisbrich et al., 2007), as well as certain motor proteins (Barisic et al., 2015; Jeffrey et al., 2016; McKenney et al., 2016; Mohan et al., 2019; Peris et al., 2009; Sirajuddin et al., 2014; Tas et al., 2017). Detyrosination is a particularly important microtubule PTM as numerous cellular processes are regulated by microtubule detyrosination, including mitosis/meiosis, intracellular transport, autophagy, neurogenesis, and cardiomyocyte contractility (Akera et al., 2017; Barisic et al., 2015; Gundersen and Bulinski, 1986; Konishi and Setou, 2009; Landskron et al., 2022; Liao et al., 2019; Mohan et al., 2019; Robison et al., 2016; Tas et al., 2017). Detyrosinated microtubules are known to persist much longer than tyrosinated microtubules in live cells (Kreis, 1987; Schulze and Kirschner, 1987; Webster et al., 1987b). It has long been proposed that this stability is not due to detyrosination itself altering the intrinsic dynamics of microtubules, but the change in interaction with many MAPs that collectively alter the microtubule dynamics (Khawaja et al., 1988; Raybin and Flavin, 1975; Webster, 1990). Indeed, a recent in vitro study employing recombinantly expressed α-tubulin lacking the C-terminal tyrosine

demonstrated that these detyrosinated microtubules are not intrinsically more stable than tyrosinated microtubules without the influence of MAPs (Chen et al., 2021).

Previously, using super-resolution microcopy, we classified microtubule sub-populations based on their PTMs in epithelial cell types and found that detyrosination only occurs on ~30% of total microtubules, while acetylation is much more predominant and constitutes ~70% of total microtubules (Mohan et al., 2019). We further showed that lysosomes and autophagosomes are enriched on this small subset of detyrosinated microtubules and that this enrichment is important in promoting their fusion. Hence, building a small subpopulation of detyrosinated microtubules that can spatially regulate organelle positioning seems to be crucial for cellular processes like autophagy. It has also been shown that in neuronal dendrites, tyrosinated microtubules are concentrated on the outer portion of the dendrite, spatially segregated from acetylated (and also presumably detyrosinated) microtubules (Katrukha et al., 2021), and the two populations were proposed to mediate motor transport in opposite directions (Tas et al., 2017). These results overall show that in several cell types including epithelial cells and neurons, detyrosinated microtubules constitute a distinct subset of all microtubules to regulate diverse cellular processes.

Because VASH prefers polymerized tubulin as a substrate compared to free tubulin dimers (Aillaud et al., 2017; Li et al., 2019; Li et al., 2020; Nieuwenhuis et al., 2017), detyrosination occurs more readily once the microtubules are assembled. On the other hand, the tubulin tyrosine ligase (TTL) adds back the tyrosine primarily on detyrosinated free tubulin dimers (Szyk et al., 2011), therefore detyrosination is likely stably present on assembled microtubules and α-tubulin does not revert to tyrosinated form until the tubulin subunit is released back to the cytosolic pool upon microtubule depolymerization. It is thought that TTL stays associated with the tubulin pool in the cytosol and sequesters tubulin dimers (Szyk et al., 2011), consistent with early work suggesting that the cytosolic tubulin pools are largely tyrosinated (Gundersen et al., 1987) and that nascently rescued stretches of microtubules are also tyrosinated (Bré et al., 1987). Additionally, early work showed that when detyrosinated tubulin dimers were injected into the cells in which most of microtubules were depolymerized by Nocodazole, they became tyrosinated relatively quickly (Webster et al., 1987a). Consequently, overall detyrosination levels respond to the change of the balance between free tubulin dimers and microtubules, i.e., total detyrosination decreases markedly upon microtubule disassembly, and increases upon microtubule stabilization (Gundersen et al., 1987; Li et al., 2019; Li et al., 2020). However, the long-standing question remains as to how a subset of highly detyrosinated microtubules emerges adjacent to completely tyrosinated ones through the action of a cytosolic detyrosinase that predominantly acts on

polymerized microtubules. Multiple models are possible, including cooperativity among the VASH enzymes especially when enzyme concentration is limited, processive motion or facilitated diffusion of the VASH enzyme along the microtubule lattice, or preferential accumulation/recruitment of the VASH enzyme to a sub-set of microtubules.

To address this long-standing question, we investigated how cells establish and propagate detyrosination on a subset of microtubules using a combination of multicolor DNA Point Accumulation in Nanoscale Topography (DNA-PAINT) (Jungmann et al., 2014) super-resolution microscopy, single molecule tracking and computational modeling. Our experimental results coupled with stochastic modeling using parameters extracted from our experiments suggest a mechanism where selective enrichment of detyrosination is a function of enzyme concentration and arises from the positive feedback between detyrosination and microtubule stabilization.

Results

Nascent detyrosination appears as disperse and isolated puncta along microtubules and increases slowly over time.

To understand how detyrosination progressively builds up in cells, we treated BSC-1 epithelial cells with Nocodazole for three hours, which leads to almost complete microtubule disassembly (Bré et al., 1987), and washed out the compound to allow the microtubules to reassemble over time. Cells were fixed every 30 minutes post washout, stained with antibodies against β-tubulin and detyrosinated α-tubulin and imaged using multi-color DNA-PAINT super-resolution microscopy (Jungmann et al., 2014). Similar to our previous study, in untreated cells, we observed detyrosination enriched on a subset of microtubules while many adjacent microtubules were completely tyrosinated (**Figure 1**). Upon Nocodazole treatment, on the other hand, the majority of microtubules, including detyrosinated microtubules disappeared as expected (**Figure 1**) (Bré et al., 1987; Gundersen et al., 1987; Li et al., 2020; Webster et al., 1987a), which allowed us to monitor how nascent detyrosination re-emerges.

At 30 min post washout the majority of microtubules were already re-assembled (**Figure 1**), whereas detyrosination was largely absent on these re-assembled microtubules. However, close examination of the super-resolution images showed that nascent detyrosination events were detectable as sparse, small puncta on some regions of microtubules (176 ± 98 nm nearest neighbor distance between puncta borders), with a median area of 1326 ± 290 nm^2 and a median length of 85 ± 12 nm (**Figures 2A-C**). At 60-90 min after washout, the frequency of the discrete detyrosinated puncta increased. Accordingly, the median distance between them decreased (163 ± 40 nm at 60 min and 109 ± 19 nm at 90 min) (**Figure 2C**), with only a slight increase of the median detyrosination length (86 ± 9.5 nm at 60 min and 98 ± 8.5 nm at 90 min) (**Figure 2B**), and the median area (1476 ± 329 nm^2 at 60 min and 1933 ± 237 nm^2 at 90 min) (**Figure 2A**). These results suggest that the puncta are isolated, stochastic nascent detyrosination events rather than growth of established detyrosination sites. At later time points (120-150 min), we found that the distance between detyrosinated puncta did not change dramatically (**Figure 2C**) while detyrosination median length (114 ± 15 -130 ± 22 nm) (**Figure 2B**), and median area (2454 ± 769 - 3174 ± 972 nm^2) (**Figure 2A**) continued to increase, which is consistent with the puncta merging together as their frequency increases to generate larger stretches of detyrosinated microtubules (**Figures 1 and 2A-C**). We also observed that the anti-detyrosinated α-tubulin antibody stained non-specifically and produced diffuse background puncta outside of microtubules. During our analysis, we excluded puncta that have a density beyond two-standard deviation from the average

as these very dense puncta tend to correspond to background signal and imaging artefacts. To determine the contribution from the remaining background signal to what we considered to be the nascent detyrosinated puncta overlapping with microtubules, we measured the false co-localization percentage of detyrosinated puncta with microtubules by rotating the two images with respect to one another (**Figure S1** and Methods). This analysis showed that the false co-localization percentage was on average only 9-20% compared to the real co-localization (**Figure S1** and Methods), with the higher false co-localization percentage corresponding to the early time points (30-90 min), when detyrosinated puncta were most sparsely located on microtubules. Given that the false co-localization percentage is overall low, especially between 120-150 minutes, we do not expect the non-specific background signal to influence our results.

Detyrosinated puncta at early time points constitute 1-3 detyrosinated α-tubulin subunits

We next wondered whether the isolated small puncta represent single or multiple detyrosinated α-tubulin subunits, which is critical to address for a mechanistic understanding of detyrosination propagation. Since the spatial resolution of our DNA-PAINT images is ~20-30 nm, whereas the size of a tubulin hetero-dimer is ~8 nm, we cannot directly resolve multiple detyrosination events happening on adjacent α-tubulin subunits. In single molecule localization microscopy (SMLM), including DNA-PAINT, images of a single protein (or fluorophore) resemble a small cluster of localizations with a broad distribution due to repeated “blinking” and non-stoichiometric antibody labeling (Gyparaki et al., 2021; Zanacchi et al., 2017). We previously showed that, if the distribution of the number of localizations corresponding to a single protein target is known, it can be fit to a lognormal distribution to obtain a calibration function (Cella Zanacchi et al., 2019; Gyparaki et al., 2021; Zanacchi et al., 2017). The calibration function can then be used to deduce the number of protein targets in the actual super-resolution clusters or puncta. To obtain a calibration function for a single detyrosination site, we carried out an antibody titration experiment (1:1000, 1:2500, 1:5000 dilution) to determine a primary antibody concentration that is low enough to sparsely detect detyrosination signal from individual α-tubulin subunits in untreated BSC-1 cells (**Figures 2D and S2**). This antibody titration approach has previously been successfully used to estimate protein copy number in super-resolution images by us and others (Cella Zanacchi et al., 2019; Ehmann et al., 2014; Gyparaki et al., 2021; Zanacchi et al., 2017).

In contrast to images stained with saturating amounts of primary antibodies (1:100) that show a continuous detyrosination signal along the length of the microtubule (**Figure 1, top row**), detyrosination under dilute antibody labeling conditions appeared as sparse, small puncta (**Figure 2D and Figure S2**). At the lowest concentration used (1:5000 dilution), there was no detectable

detyrosination signal on microtubules (**Figure S2A**). We could detect detyrosination signal with 1:2500 and 1:1000 dilution (**Figures S2B and S2C**), with the 1:1000 dilution generating detyrosinated puncta that contained a slightly higher number of localizations (median 23 vs 16) that were more closely spaced together (median distance 147 nm vs 386 nm) than the 1:2500 dilution (**Figures S2B and S2C**). We thus used the sparser 1:2500 dilution as the calibration data for a single detyrosination site. We plotted the frequency distribution of the number of localizations in each detyrosinated puncta obtained from the calibration images and fit it to a lognormal distribution to obtain the fit the mean (μ) and variance (σ) (**Figure 2E**). We then fit the frequency distribution of the number of localizations from the Nocodazole wash out experiments to a linear convolution of the lognormal calibration function to estimate the number of detyrosinated subunits in these images (**Figure 2F**). Our results showed that the puncta at early time points after Nocodazole washout corresponded to 1-3 detyrosinated sites and the proportion of single, double, and triple detyrosinated sites changes over time. In particular, the puncta at 30-60 min after Nocodazole washout were predominantly (~60%) single detyrosinated sites with only a minor population of 2 and 3 detyrosinated sites (**Figure 2F**). At 90 min, the proportion of puncta containing single detyrosinated sites decreased and the proportion of puncta containing 3 or more detyrosinated sites increased (**Figure 2F**). These results further suggest that nascent detyrosination occurs at a limited (mostly single) number of subunits sparsely and sporadically distributed along the length of the microtubule.

Previously, we showed that the majority of detyrosinated microtubules are also acetylated, although acetylated microtubules constitute a much higher proportion of the total microtubule network (Mohan et al., 2019). Acetylation occurs on Lys40 on α-tubulin, which is located in the microtubule lumen. To compare the kinetics of acetylation to those of detyrosination, we repeated the Nocodazole washout experiments and stained for acetylated tubulin. The recovery of acetylation after Nocodazole washout occurred much faster than detyrosination. We observed a significant amount of long stretches of acetylation along microtubules at 15 min post Nocodazole washout, and by 30-60 min, a large proportion of microtubules were already acetylated along their entire length (**Figure S3**). These results are consistent with previous reports (Ly et al., 2016) and in contrast to our results with detyrosination, which starts at sparse, limited sites and accumulates with much slower kinetics in cells.

Single molecules of VASH bind to microtubules stochastically and show distinct mobility modes.

Our super-resolution data suggest that detyrosination occurs stochastically and on only a few subunits at a time on microtubules. To further support this mechanism, we turned to single molecule imaging of the major carboxypeptidase, Vasohibin (VASH) (Aillaud et al., 2017; Nieuwenhuis et al., 2017), in live cells. Mammals have two isoforms of VASH, VASH1 and VASH2, both of which constitutively complex with the small Vasohibin-binding protein (SVBP) (Suzuki et al., 2010) which is a 66-amino acid peptide containing mainly an alpha helix. The two VASH isoforms share conserved structures, including their catalytic cores, although the molecular details comparing their enzymatic activities and mode of actions have not been reported so far.

To determine how individual VASH proteins interact with microtubules in live cells, we co-expressed human SVBP-Myc-FLAG and human VASH1 or VASH2 with a C-terminal Halo Tag from a lentiviral vector in the human U2OS cells, the microtubules of which are largely tyrosinated (Kesarwani et al., 2020). Detyrosination significantly increased upon ectopic WT VASH expression compared to uninfected cells (**Figure 3A**), demonstrating that the VASH-Halo/SVBP complex is active. To track single molecules of VASH, we labeled Halo-tag with its ligand conjugated with JF549 (Grimm et al., 2015). We further labeled microtubules in live U2OS cells with Tubulin tracker (**Figure S4A**) and used the microtubule images as a mask to discard cytosolic VASH molecules that did not overlap with microtubules and only analyzed those trajectories that substantially overlapped with labeled microtubules (**Figures 3B and S4B**). As the microtubule image was recorded as a snapshot prior to the single molecule tracking and the end of the single molecule movie is shifted in time by 130 seconds from the microtubule snapshot, we checked for the stability of the microtubules during this time period (**Figure S4A**). Most regions of the microtubule network overlapped but some microtubules showed a modest amount of shift in this time period. Hence, to account for the shift, we considered trajectories that had a minimum of 20% overlap with the microtubule mask to be microtubule associated (Methods).

As observed previously, VASH was predominantly cytosolic (**Figure S5**) (Aillaud et al., 2017; Nieuwenhuis et al., 2017). However, those trajectories that overlapped with the microtubule mask showed two types of behavior. A proportion of VASH molecules exhibited diffusive behavior on microtubules, sometimes moving bi-directionally for short time periods along a single microtubule (**Figures 3C and S4C, Supplementary Movies S1 and S2**). In some cases, we observed prolonged diffusion of VASH along microtubules, in particular in regions where multiple microtubules crisscrossed (**Figure S4D and Supplementary Movies S3 and S4**). A second population of VASH molecules exhibited highly confined motion at a given spot on microtubules for a short period of time before diffusing out of focus (**Figures 3C and S4C, Supplementary**

Movies S5 and S6). In some select cases, we observed switching behavior between Brownian and confined motion in a single trajectory (**Figure S4E, Supplementary Movie S7**). We carried out mean square displacement analysis for trajectories that contained more than 10 frames (or 0.5 s in tracking time) and classified the motions of VASH WT enzyme molecules into three categories: confined (having an MSD alpha coefficient ≤ 0.8), Brownian (having an MSD alpha coefficient between 0.8-1.5) and directed (having an MSD alpha coefficient ≥ 1.5). The directed trajectories constituted a minimal proportion of all trajectories (2-3%) (**Figures 3D and 3E, Table 1**). These trajectories were also mostly short lived and are likely due to tracking errors or mis-classification due to limitations of the MSD analysis. Interestingly, roughly equal proportion of VASH molecules exhibited Brownian (59.7%, 56.1% for VASH1 and VASH2 respectively) or confined motion (35.9%, 40.6% for VASH1 and VASH2 respectively) on microtubules (**Figure 3E, Table 1**).

To determine the dwell time of the VASH molecules on microtubules, we fit the residence time for Brownian and confined trajectories to a double exponential. We took the long time constant after photobleaching correction (**Figure S4F** and see Methods) to represent the specific interaction of VASH with microtubules as is standard in single molecule tracking experiments (Ball et al., 2016; Chen et al., 2014; Gómez-García et al., 2021). The Brownian residence time was 1.29 s for VASH1, and 1.70 s for VASH2, and the confined residence time was 2.53 s and 3.00 s for VASH1 and VASH2, respectively (**Figures 3F and 3G, and Table 1**). These results show that in both cases, the residence time is brief, and VASH interacts only transiently with microtubules. Based on the previously reported K_{cat} of VASH1 (Li et al., 2019), which is 44.5/min (or 0.74/sec), the dwell time of both motion types only allows 1-2 catalytic cycles per interaction with the microtubule, which is consistent with our estimation of the number of detyrosinated sites in nascent detyrosinated puncta in super-resolution images of Nocodazole washout cells (**Figure 2F**). In addition, in our single molecule tracking videos, especially in cells with relatively high expression of VASH, the VASH trajectories appeared to overlap with most if not all microtubules (**Figure S4G**). We have also observed that the number of detyrosinated microtubules was much higher in VASH-EGFP overexpressing cells compared to untransfected cells (**Figure S5**) and Taxol treatment also drastically increased both the kinetics of detyrosination and the percentage of detyrosinated microtubules (82 ± 25 % total microtubule after 3 hr Taxol treatment, **Figure S6**), which is consistent with previous literature (Aillaud et al., 2017; Landskron et al., 2022; Wang et al., 2019). Overall, these results support that VASH can bind and interact with all microtubules. Further, we did not observe multiple VASH molecules binding to the same region consecutively, which is also consistent with the super-resolution data and suggests that microtubule binding

cooperativity is likely not the dominant mechanism for detyrosination to build up continuously on a microtubule.

It is possible that VASH molecules may distinguish the detyrosinated versus tyrosinated α-tubulin tails on the microtubules, which may promote a preference for VASH to bind and dwell longer on microtubules with more tyrosinated tubulins to allow more catalytic cycles. To test this possibility, we carried out single molecule tracking experiments of VASH1 and VASH2 at 30 min post Nocodazole washout, when microtubules are largely reassembled but detyrosination is still mostly absent (**Figure 1**). We found that the percentage of Brownian and confined motions of either VASH1 or VASH2 were similar at 30-minute Nocodazole washout to the conditions where detyrosination has been established (**Figure S7, Table 1**). The residence time of Brownian (1.34 and 1.70 sec for VASH1 and VASH2) and confined (1.38 and 2.23 sec for VASH1 and VASH2) motions were also comparable and if anything, slightly shorter than those from cells that have more established detyrosination (**Figure S7, Table 1**). This suggests that VASH does not dwell longer on more tyrosinated microtubules in cells.

A microtubule binding mutant of VASH2 exhibits reduced dwell-time on microtubules.

Numerous correlative structural and functional experiments demonstrated specific mutations that separate VASH's microtubule-binding from its free tubulin tail binding or its catalytic core. (Adamopoulos et al., 2019; Aillaud et al., 2017; Li et al., 2019; Li et al., 2020; Nieuwenhuis et al., 2017; Suzuki et al., 2010; Wang et al., 2019; Zhou et al., 2019). To probe what factors can affect VASH's residence time, we tested a previously reported VASH2 mutant (VASH2 4A) that is defective in microtubule-binding and has reduced detyrosination efficiency (**Figures 3A and 3F-G**) (Wang et al., 2019). Single molecule tracking of this mutant showed that the defect in microtubule binding resulted in a significant decrease in the residence time of both confined and Brownian trajectories (**Figures 3F and 3G**) without changing the proportion of each motion type (**Figure 3E**). These results suggest that having a long enough dwell time on the microtubule is important for VASH's ability to efficiently detyrosinate α-tubulin tails. Given that the decrease of bulk detyrosination level in V2 4A is much more pronounced than the decrease we observed in residence time (**Figures 3A and 3G**), it is possible that the on rate of this mutant is also lower compared to the WT. However, we cannot determine the association rate constant (k_{on}) of VASH as this rate constant is concentration dependent and the concentrations of VASH in individual cells are unknown. Interestingly, we have also found that the VASH1 residence time is modestly lower compared to VASH2 in both confined and Brownian motions (**Figures 3F, 3G and S7,**

Table 1), and that the relative detyrosination efficiency of VASH1 is also modestly lower than VASH2 (~0.7 to 1, **Figure 3G**).

We further tested whether catalytic activity is crucial for VASH's dwell time and interaction with microtubules. We tracked the single molecules of the catalytically inactive mutant VASH2 C158A (V2 C158A), which is virtually incapable of detyrosinating microtubules (**Figures 3A and 3G**) (Wang et al., 2019; Zhou et al., 2019). The percentage of Brownian and confined motions of the V2 C158A was similar to WT VASH2 as were the residence time of Brownian and confined trajectories (**Figures 3E and 3F-G, Table 1**). These results suggest that VASH molecules do not change their mode of interaction with microtubules regardless of whether they catalyze detyrosination events.

Simulations support that a detyrosination-stabilization feedback mechanism can generate a subpopulation of microtubules enriched with detyrosination

Collectively, both super-resolution microscopy and single molecule tracking experiments suggest that detyrosination is largely limited to only a few subunits at a time and occurs stochastically on microtubules. If detyrosination is established through stochastic and short-lived interactions between VASH enzymes and the microtubule network, it remains unclear how only a small subset of microtubules become enriched in detyrosination along their length. It has been shown that, through interaction with MAPs, detyrosinated microtubules become more stable. A previous in vitro reconstitution study showed that the level of microtubule dynamicity scales with the level of tyrosination (Chen et al., 2021). Given that globally stabilizing microtubules in cells using Taxol accelerated the kinetics of detyrosination and increased the overall detyrosination levels (~ 3-fold increase, **Figure S6**) (Landskron et al., 2022; Li et al., 2020; Nieuwenhuis et al., 2017), we hypothesized that the enrichment of detyrosination on a subset of microtubules starts from a stochastic process, but as a result of stochastic variations in the levels of detyrosination among individual microtubules, a subset of microtubules may become more stabilized than others. Consequently, this more stable sub-population of microtubules may accumulate more detyrosination, while the remaining microtubules turnover more readily and lose detyrosination. This feedback between detyrosination and stabilization can then lead to the appearance of aged, highly detyrosinated microtubules among young, tyrosinated microtubules.

Because the stability and detyrosination level of the microtubules cannot be readily determined and tracked simultaneously in live cells, we turned to simulations to assess whether a stochastic

model with detyrosination-dependent microtubule stability can recapitulate experimentally observed detyrosination properties. Instead of mean-field kinetic models, which report only bulk microtubule dynamics (Dogterom and Leibler, 1993; Grignard et al., 2022), we developed a computational model which additionally allows us to visualize the 3D spatiotemporal features of microtubule detyrosination by explicitly simulating the dynamics of individual microtubules, enzymes and the detyrosination states of the α-tubulin subunits. In our system (**Figure 4**), the microtubule (green) minus ends were stably embedded in the inner sphere representing the centrosome (pink) and the plus ends experience dynamic instability through Monte Carlo simulations (Buttenschön and Edelstein-Keshet, 2019; Cassimeris et al., 2018) within the outer spherical boundary representing the cell plasma membrane (green). Simultaneously, VASH molecules (small diffusing spheres) simulated via reactive Brownian dynamics, are capable of binding, unbinding and detyrosinating individual microtubules (**Figure 4 and Supplementary Movie S8**).

Parameters and assumptions of the simulations

Based on prior literature, our simulations assume the detyrosinated α-tubulins are stably present on the microtubule until it is released from the microtubule upon disassembly, and all nascently assembled microtubules, including the rescued segments are initially tyrosinated. Consequently, detyrosination level fluctuates as the microtubule plus ends experience dynamic instability. To the best of our knowledge, there is no established, quantitative model describing how stability evolves as detyrosination increases on a microtubule at the molecular level. We assumed that once an α-tubulin subunit is detyrosinated on a microtubule, the catastrophe and shortening rates of that individual subunit become reduced by a certain factor (~65 % catastrophe frequency and ~53 % shortening rate of the tyrosinated subunits), along with minor changes in rescue frequency and growth rate (see Table 2, purple letters). Therefore, the plus end dynamics transition to a more stable regime each time the plus end encounters detyrosinated subunits as it grows and shrinks. The percentage changes in the catastrophe and shortening were based on the ratios we obtained from a previous study that characterized these parameters for both dynamic and stable populations of microtubules in the same cell type (Shelden and Wadsworth, 1993).

The simulated probabilities of diffusive versus confined movement of VASH were based on the fractions of each motion class from our single molecule tracking data, and we assumed that VASH detyrosinated a subunit when confined on a microtubule, with a catalytic probability derived from the enzyme catalytic rate (0.74 s^{-1}, (Li et al., 2019)). The probability of VASH dissociation was based on the enzyme off-rate (1/residence time) and subsequently the binding probability was

calculated based on the previously measured k_d (0.16 µM, (Wang et al., 2019)) between VASH and Taxol-stabilized microtubules. A complete list of parameters used in our simulations is shown in **Table 2.**

Microtubule dynamics influences detyrosination kinetics and total detyrosination levels

A fundamental aspect of our positive feedback hypothesis is that stable microtubules accumulate more detyrosination. Hence, we first tested whether different microtubule dynamicities will result in different total detyrosination levels using our simulations. We thus carried out three different sets of simulations, each simulating a different set of dynamic parameters representing highly dynamic (set A), intermediately dynamic (set B), or fully stable microtubules (set C, **Table 3** and **Figure S8**, (Cassimeris et al., 2018)). In both set A and B, upon detyrosination, the microtubule subunit will transition to a more stable regime as described above (**Table 2)**. For set C, plus-ends were fixed at the outer cell boundary and detyrosination has no effect on stability.

At a concentration of ~ 100 nM of VASH, we found that the total percentage of detyrosination scales linearly with time and the stability of the microtubules impacts both the kinetics and the total levels of detyrosination (**Figure 5A**). This linearity was well captured by a simplified analytical model of detyrosination (**Figure 5A**, **dashed lines**, Methods). To compare to our experimental data, we blurred our simulation resolution (0.6 nm) to the typical resolution of DNA-PAINT imaging (~30 nm, about 50-fold lower resolution than the simulation) (**Figure 5B, and Methods**), and we refer to individual blurred detyrosination subunit as a punctum, similarly termed as in our super-resolution images. The kinetics of detyrosination in our experiments (**Figure 5B, dark blue diamonds**) matched most closely to the highly dynamic microtubules (set A, **Figure 5B**), although our experimental data showed more heterogeneity from cell to cell, likely reflecting variations in dynamicity of microtubules and/or enzyme concentrations. The size, length and the distance between detyrosinated puncta from highly dynamic microtubules in our simulations also showed similar characteristics to our experiments. At a total ~ 0.25 % detyrosination level, which is close to the total level at the 30-min Nocodazole washout, we measured nascent detyrosination puncta (**Figures 5C-E**) having a median area of 1292 nm^2, a median length of 84.85 nm, and a median border-to-border distance of 342 nm. As the total detyrosination level rises to 2.5 %, the median puncta area (1460 nm^2) and length (94.8 nm) increase, whereas median distance between puncta declines (247.4 nm) (**Figures 5C-E**), similar to our washout experiment. Altogether, our simulations produced results that match our experimental observations regarding the nascent puncta characteristic and early detyrosination kinetics, and validated the observation that increased microtubule stability (as in microtubule set C) enhances detyrosination on microtubules.

The steady state in which there exists a subpopulation of microtubules highly enriched in detyrosination and where detyrosination and tyrosination are at equilibrium likely occurs much later than 150 min post Nocodazole washout as at this time point, the super-resolution images still show punctate and sparse detyrosination. In our simulations, while the 100 nM VASH concentration captured the early kinetics of detyrosination build-up, this low enzyme concentration required impractical simulation time to reach steady state detyrosination levels. To overcome this challenge and compare the steady state detyrosination patterns to our experiments, we therefore increased the amount of VASH to accelerate the process. At 1-5 µM VASH concentration (**Figure S9**), steady states were reached within 1 hour (real time), and the bulk detyrosination levels plateaued at around 23% and 52% for highly dynamic and intermediately dynamic microtubules, respectively. Fully stable microtubules reached almost full level (94%) of detyrosination after 10,000 s (navy blue), similar to experiments that showed close to fully detyrosinated microtubule network after 3 hours of Taxol treatment (82 ± 25%, **Figure S6**). The plateau behavior we observed at steady state deviates from the linear increase of detyrosination at early time points (**Figure 5B**) and the linear increase predicted by our analytical theory. This is because (1) the detyrosination and tyrosination reached equilibrium and (2) when resolution was blurred, detyrosinating additional subunits inside an existing detyrosinated punctum did not further increase the punctum area. As a result, detyrosination curves are expected to flatten out even for fully stable microtubules (**Figure S9**).

Overall, the simulations recapitulate the early accumulation of detyrosination in the form of stochastic, sparse puncta and the leveling off of the detyrosination levels at steady state.

Enrichment of detyrosination arises from stochasticity, high dynamicity of microtubules and stabilization feedback

We next took advantage of our spatiotemporal model to test whether detyrosination becomes highly concentrated on a subpopulation of microtubules. At a total detyrosination level of 23.3 ± 0.5%, we observed a wide distribution of detyrosination levels on individual microtubules within a single simulation (**Figure 6A**). Histograms of detyrosination percentages on microtubules before and after resolution blurring both showed increased heterogeneity with increased microtubule dynamics. Also, we started observing microtubules that have close to zero detyrosination (≤ 15 %, blue dashed boxes in **Figure 6A**) and those that have close to full detyrosination (≥ 75 %, green dashed boxes in **Figure 6A**) particularly in the dynamic microtubules. The stable microtubules showed the least variation in detyrosination distribution and reduced number of microtubules with low (≤ 15 %) detyrosination levels (**Figure 6A**). This suggests that high dynamicity coupled with

increased stability as a result of detyrosination, unexpectedly, promotes the emergence of detyrosination enrichment on some but not all microtubules. A close examination of the progression of the detyrosination on highly dynamic microtubules showed that microtubule plus end dynamics significantly slowed down depolymerization because of detyrosination, which gives rise to more persistent microtubules. In the region shown in **Figure 6B**, a highly detyrosinated microtubule persisted for 11 minutes (**Figure 6B,** white arrows) whereas a sparsely detyrosinated microtubule lasted only 1.3 minutes (**Figure 6B**, magenta arrows), giving rise to the phenomenon of aged, highly detyrosinated microtubules co-existing with young tyrosinated ones (**Figure 6B**, bi-directional arrow).

Overall, our study supports a model (**Figure 7**) that detyrosination occurs stochastically on microtubules, and the detyrosination-dependent microtubule stability reinforces further accumulation of detyrosination, forming positive feedback to build a stable, and highly detyrosinated microtubule subset.

Discussion:

Numerous PTMs are found in selected subsets of microtubules in cells, and how microtubules are segregated into these functional subpopulations has been a long-standing question (Roll-Mecak, 2019). Detyrosination is among the first microtubule PTMs (Arce et al., 1975; Barra et al., 1973) that were identified and, unlike other PTMs such as acetylation, detyrosination can be highly compartmentalized to bias organelle transport mediated by motors (Katrukha et al., 2021; Mohan et al., 2019). Using a combination of quantitative super-resolution, live cell single molecule tracking and spatiotemporal stochastic simulations, we propose that detyrosination is concentrated on a small subset of microtubules through a stabilization-detyrosination feedback mechanism starting from a stochastic process. Early after nocodazole washout, the quantitative DNA-PAINT super-resolution images provided us the insight that detyrosination occurs primarily on one α-tubulin tail at a time (~60% of all initial sites contain a single detyrosinated subunit) and these initial detyrosinated sites are many tubulin subunits away from each other (median distance, 179 nm) (**Figure 2**). Regardless of the type of enzyme that is at play, these results suggest that consecutive or cooperative detyrosination on the microtubules is not prevalent, instead, detyrosination is sporadic. Furthermore, throughout the time course post washout, the proportion of single detyrosinated sites decreased but persisted and these sites appeared closer to each

other, suggesting that continuous detyrosination in untreated cells results from the merging of separate, single detyrosination events as they appear more frequently with time.

We tracked VASH as the primary detyrosinase, which contributes to the majority of total detyrosination in many cell lines and in the mouse brain (Aillaud et al., 2017; Landskron et al., 2022; Nieuwenhuis et al., 2017). These data showed that the brief interaction of VASH with the microtubule only allows 1-2 catalytical cycles for VASH to detyrosinate, which is consistent with the results from our super-resolution quantification. In all our experiments, VASH1 and VASH2 do not show major differences except that VASH2 expression results in modestly higher detyrosination than VASH1 (**Figure 3A**), and accordingly, VASH2 consistently has a slightly longer dwell time in all motion categories (**Figures 3F and 3G**, Table1). These results are consistent with previous literature showing conserved structures between these two isoforms. Interestingly, about half of the total trajectories are diffusive on microtubules, and given the slow catalytic rate of VASH (0.74 s^{-1} for VASH1 (Li et al., 2019)) and the limited number of detyrosination events found in detyrosination puncta in our super-resolution images, these diffusive events that span many tubulin subunits within 1-2 seconds are unlikely the detyrosinating events. We interpret that VASH, through the diffusion, surveys the microtubule surface to locate a substrate, as we have observed a small fraction of trajectories that transition from diffusive behavior to confined behavior (**Figure S4E** and **Supplementary Movie S7**). Such “facilitated 1D diffusion” mechanism has previously been suggested to help transcription factors find their binding sites within chromatin more rapidly compared to 3D diffusion (Izeddin et al., 2014; Normanno et al., 2015). Similarly, diffusion along the microtubule can potentially help reduce VASH’s search time for a target site. So far, it is unclear what governs VASH to be confined as opposed to diffusing along the microtubule lattice. We have found no evidence suggesting that VASH changes its behavior if the α-tubulin tail is already detyrosinated, because we observed similar proportion of diffusive and confined motions when we tracked VASH early after nocodazole washout, when microtubules are mostly tyrosinated. It is possible that MAPs present on microtubules may influence whether VASH can be stably bound to one α-tubulin tail for the amount of time the enzyme requires for detyrosination. For example, a recent study suggested that presence of MAP4, but not phosphorylated MAP4, on microtubules may block the local access of VASH2 in cardiomyocytes (Yu et al., 2021). A previous cryo-EM study showed that VASH, presumably stably bound to microtubules, engages with two α-tubulins from two adjacent protofilaments (Li et al., 2020), and structural studies also suggested that the C-terminal tail of α-tubulin is supposedly occupied by the catalytic pocket of VASH for detyrosination to occur (Li et al., 2019; Li et al., 2020; Wang et al., 2019; Zhou et al., 2019). Yet, it is unclear how VASH

molecules interact with microtubules during diffusive movement and whether presence of MAPs affect the motion type of VASH.

In our simulations, we constructed an idealized system incorporating the two main mechanisms, the stochastic detyrosination and the stabilization of microtubules by detyrosination. While similar approaches have been employed to characterize diverse biological processes involving molecular recognition, such as the search of regulatory proteins for specific DNA-binding targets (Brackley et al., 2013; Mirny et al., 2009) and the clustering of chemotaxis sensing complexes (Schöneberg et al., 2014; Ullrich et al., 2015), to the best of our knowledge, this is the first implementation of reaction-diffusion algorithms to characterize how dynamic microtubules are modified by an enzyme over time with 3D spatial resolution. Our simulations captured the nascent detyrosination kinetics shown by our experiments and showed that the levels and kinetics of detyrosination are dependent on microtubule stability. We also observed the appearance of “old” microtubules highly enriched in detyrosination next to “young” tyrosinated microtubules. These results support that in the stochastic system, the dynamicity of the tyrosinated microtubules and the stability feedback mechanism together promote the enriched detyrosination (**Figures 6**).

In our simulations, we also observed partially detyrosinated microtubules even at steady state detyrosination levels, which were not observed experimentally in epithelial cells. This discrepancy could be due to a couple of reasons. First, it is possible that we under-estimated the amount of the stability conferred by detyrosination to microtubules in our model. Indeed, stability of a detyrosinated subunit was only a factor of ~2 higher than a tyrosinated subunit in our simulations, which is an assumption of our model. Second, we assumed that stability is conferred at the subunit level. In our model, a microtubule with a detyrosinated subunit close to the plus end will not depolymerize as readily as a microtubule with a detyrosinated subunit close to the minus end, despite having similar levels of detyrosination. Yet, there can be alternative molecular mechanisms for detyrosination-dependent stabilization of microtubules and it is not clear if there is a threshold level of detyrosination that needs to accumulate for a microtubule to have increased stability. Decades of literature have provided highly variable, cell type-dependent measurements for the catastrophe and shortening rates of microtubules. This is likely due to various factors, including concentration of VASH and MAPs, and the composition of MAPs, which likely account for the cell type-dependent degree of stability. These variables may impact how restricted or widespread detyrosination is depending on the cell type. Indeed, it has been observed that unlike in epithelial cells or neurons, some other cell types do not have distinct detyrosinated versus tyrosinated microtubule populations, but rather partial detyrosination on many microtubules like

in our simulations (Robison et al., 2016). This cell type variation in detyrosination distribution could be due to variable cellular concentrations of VASH, MAPs, and MAP type dependent mechanisms of microtubule stabilization. It would be valuable to simulate detyrosination process with alternative models for microtubule stabilization, which may generate testable predications for future experiments.

On the other hand, certain microtubules may become more stable independent of the pre-existing detyrosination level to further lead to accumulation of detyrosination, which likely enhances the enrichment of detyrosination on a subset. It has been shown that minus-end stabilization proteins, such as CAMSAP2, rapidly associate with nascent microtubule minus ends and promote more detyrosination (Jiang et al., 2014), consistent with the feedback model.

It is interesting to postulate whether this feedback mechanism can explain enrichment of other PTMs on subsets of microtubules, for example, stable microtubules are also enriched in acetylation and glutamylation (Janke and Magiera, 2020; Roll-Mecak, 2019). Incorporating the results and simulations from our study, we reason that the microtubules which persist longer will allow the time-dependent accumulation of PTMs if polymers are the preferred substrate and the enzyme acts on a time scale that is much slower than the inherent stable periods of the microtubules. Additionally, we found that the enzyme concentration can strongly influence the outcome when the enzyme is diffusion limited. In our study and a previous report (Ly et al., 2016), L40 acetylation is re-established in the cells much faster than detyrosination after nocodazole washout and acetylation is also much more prominent than detyrosination, occurring on 70% of all microtubules. Previous in vitro work indeed showed that acetylation, similar to what we find for detyrosination in cells, is stochastic and that TAT can access and enter the microtubule lumen not only through microtubule ends but also within the microtubule lattice (Szyk et al., 2011). These results are consistent with the cellular patterns of widespread acetylation and suggest that two different stochastically acting enzymes can give rise to differential modification kinetics and different levels of modified microtubules, likely by tuning the enzyme concentration, the enzyme catalytic rate and the enzyme binding time to the microtubule with respect to the timescale of microtubule stability. It is also possible that since acetylation happens in the microtubule lumen, in cells, TAT becomes trapped inside the microtubule and that this confinement helps build continuous stretches of acetylation (Ly et al., 2016). It has been shown that glutamylation is more efficient on the microtubule polymer as well (Audebert et al., 1993), however, the relationship between glutamylation and stability is complex, for example, polyglutamylation regulates microtubule severing mediated by spastin in a biphasic manner, therefore at an intermediate level,

polyglutamylation results in less stable microtubules whereas high level polyglutamylation stabilizes microtubules (Audebert et al., 1993; Lacroix et al., 2010; Shin et al., 2019; Valenstein and Roll-Mecak, 2016). Since Tubulin PTMs play diverse roles and that the modifying enzymes have different catalytic rates (reviewed in (Roll-Mecak, 2019)), the proposed feedback mechanism between PTMs and microtubule stability in our study provides a general framework for determining the kinetics, steady-state levels and patterns of modified microtubules in different cell types. Our experimental and computational approach should provide useful in studying how various PTMs are established in the cellular context.

Figures

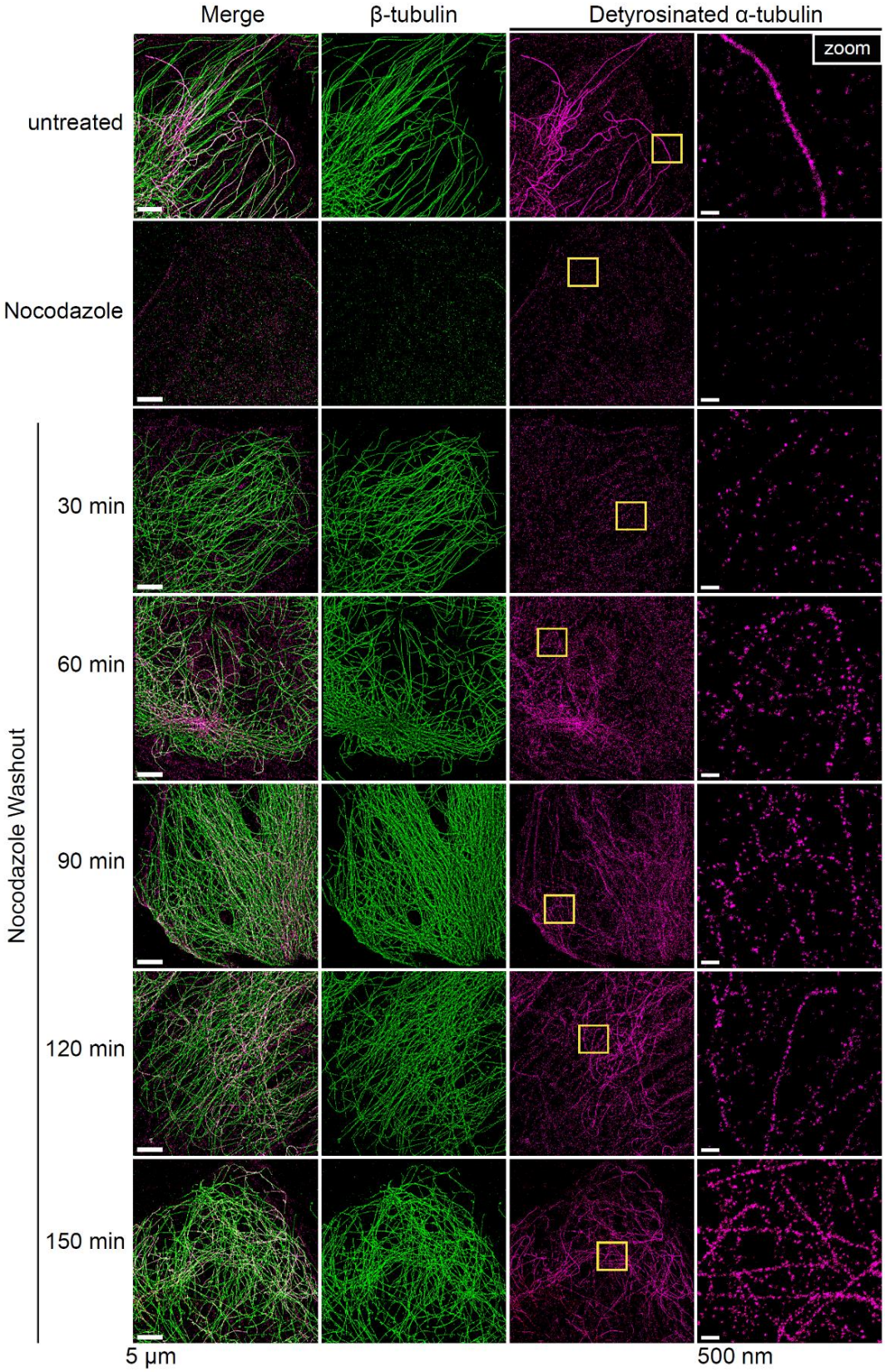
Merge
β-tubulin
Detyrosinated α-tubulin
zoom
untreated
Nocodazole
Nocodazole Washout
30 min
60 min
90 min
120 min
150 min
5 µm
500 nm

Figure 1: Super-resolution reveals detyrosination is established gradually from small, disperse puncta over time.

Representative two-color DNA-PAINT images showing detyrosinated α-tubulin (magenta) and β-tubulin (green) in fixed BSC-1 cells that are treated with 0.1% DMSO (untreated), or 33 μM Nocodazole for 3 hr at 37 ºC, and at 30-, 60-, 90-, 120-, 150-min after the Nocodazole washout. Yellow boxes indicate the regions selected for the zoom images on the right most column. Scale bars, 5 μm. Scale bars in zoom, 500 nm.

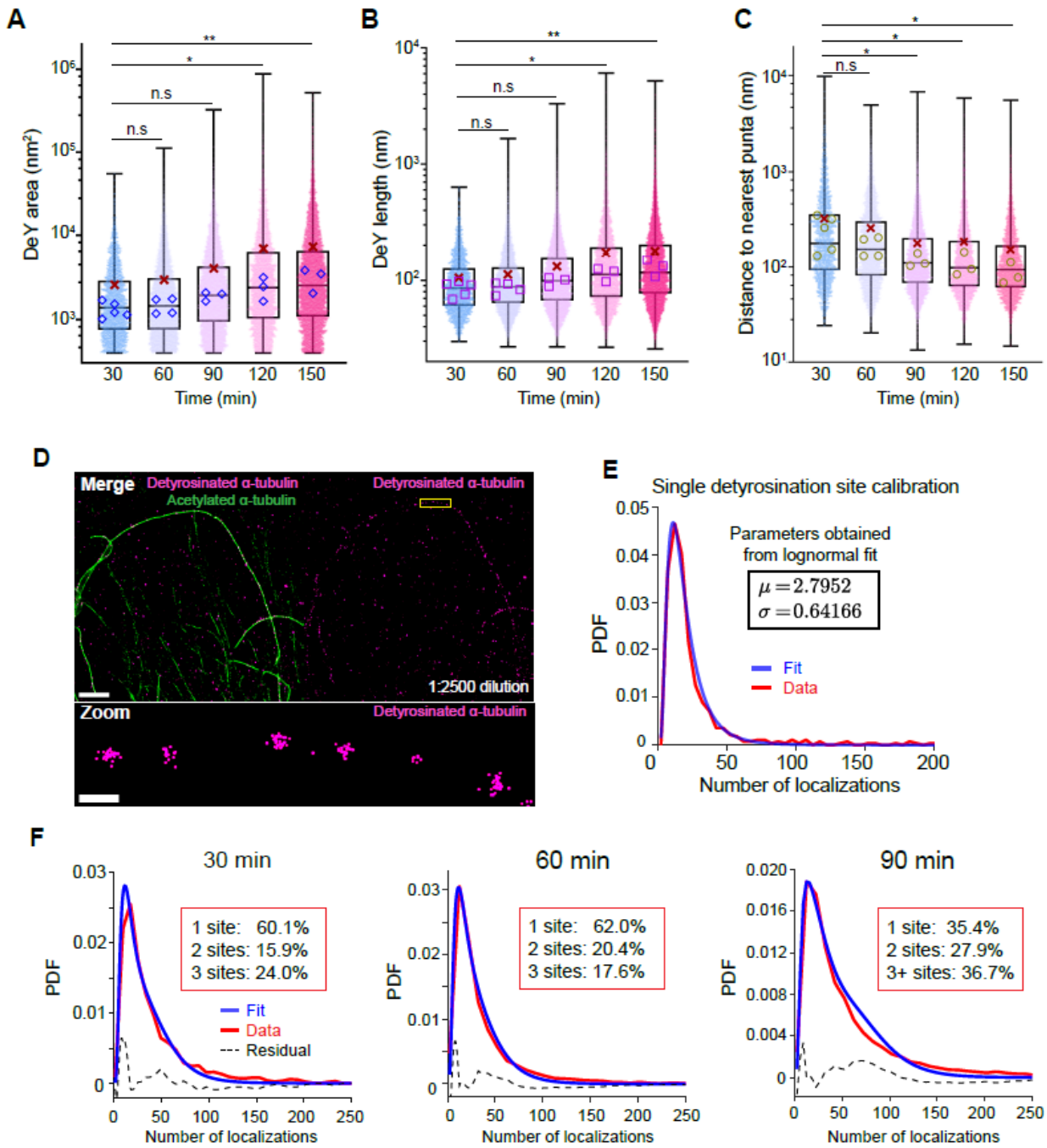

Figure 2: Diffraction limited, nascent detyrosinated puncta correspond to 1-3 detyrosination sites accumulate slowly over time and merge into larger detyrosinated areas.

Superplots showing quantitative measurement of detyrosination cluster area (**A**), length (**B**), and the distance to the nearest neighbor cluster (**C**) at each time point after Nocodazole washout shown in Figure1. Many detyrosination events have the appearance of small puncta at early time

points (30-min to 60-min), but appear larger and closer to each other at later time points. The measurement of individual puncta at each time point were pooled from multiple independent experiments. The scatter plot was overlaid with box and whisker showing 25th, 75th percentiles as well as the median values corresponding to each independent experiment (open blue diamonds in (**A**), open purple square in (**B**) and open brown circle in (**C**)). The red crosses indicate the mean values of all data points from each time point. For the statistics of each time point after Nocodazole washout 30 min, n = 2204 puncta, N=15 cells from 5 experiments; 60 min, n = 7846 puncta, N =17 cells from 4 experiments; 90 min, n = 10686 puncta, N = 17 cells from 3 experiments; 120 min, n =5957 puncta, N = 13 cells from 3 experiments; 150 min, n = 7631 puncta, N = 9 cells from 3 experiments. One-way ANOVA and Dunnett's multiple comparison were performed on median values from individual experiments. **P < 0.01, *P < 0.05, n.s, P > 0.05. (**D**) A representative two-color DNA-PAINT super-resolution image used for the purpose of single-detyrosination site calibration, showing detyrosinated α-tubulin and acetylated α-tubulin in untreated BSC-1 cells. Detyrosination appears as small puncta instead of being continuous because the primary antibody was used at 1 to 2500 dilution, a concentration that is 25-fold lower than the saturating amount used in Figure 1. Scale bar in the merge, 2 µm, scale bar in zoom, 200 nm. (**E**) The number of localizations per puncta in images from (**A**) was plotted as a histogram (red) and fitted to a lognormal calibration function (blue, see Methods). The mean (μ) and variance (σ) extracted from the fit are shown. A total of 559 puncta from two experiments were pooled. (**F**) Percentage of puncta having single-, double-, triple or more detyrosinated sites was obtained by the fit of the experimental data for the number of localizations per puncta (red) to a weighted convolution of single, double, triple (or more) calibration functions. The weights were extracted as the percentages. Black dotted lines show the residuals from the fit.

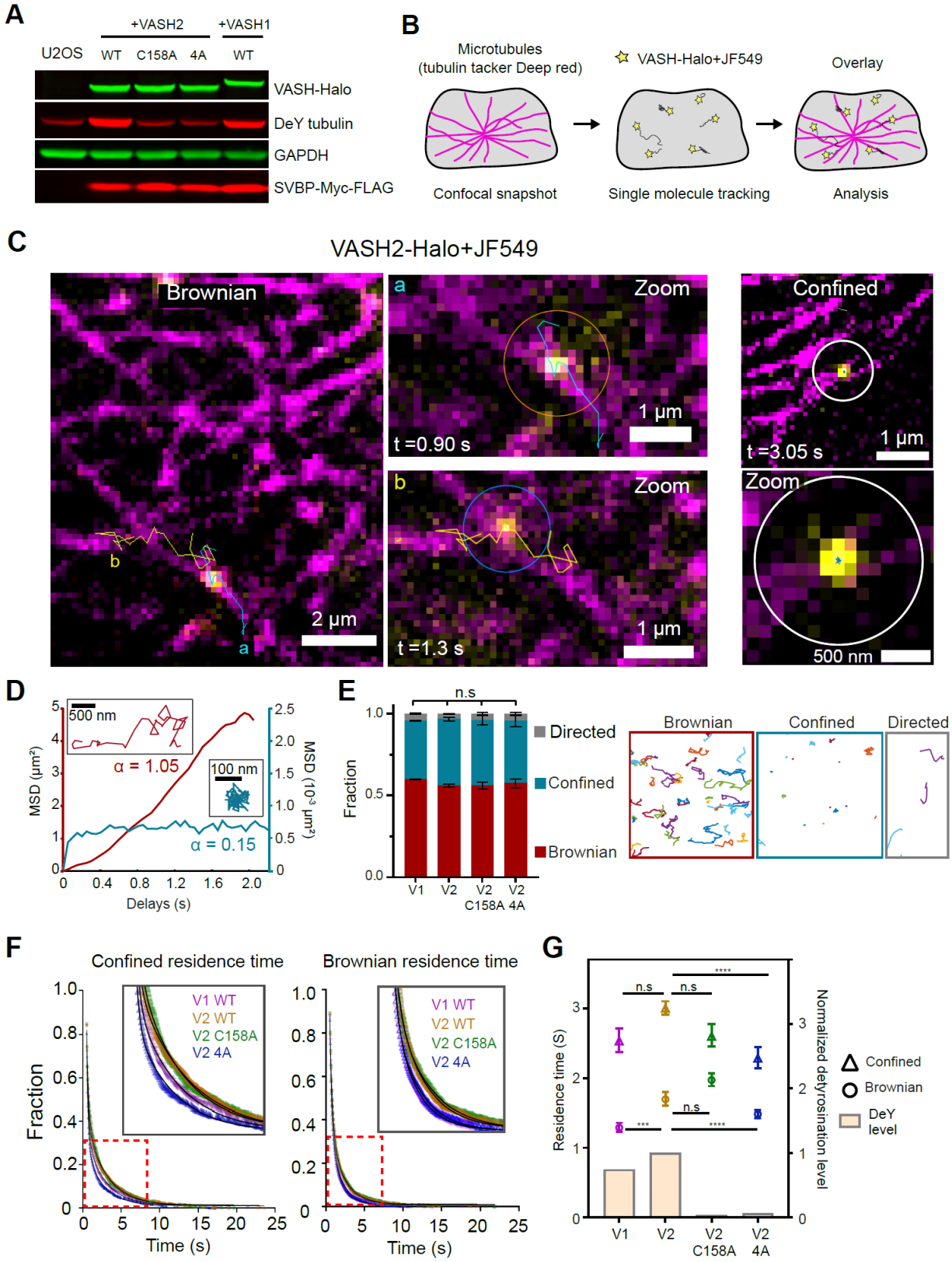
A
+VASH2
+VASH1
U2OS
WT
C158A
4A
WT
VASH-Halo
DeY tubulin
GAPDH
SVBP-Myc-FLAG
B
Microtubules
(tubulin tacker Deep red)
VASH-Halo+JF549
Overlay
Confocal snapshot
Single molecule tracking
Analysis
C
VASH2-Halo+JF549
Brownian
Zoom
Confined
1 µm
t =0.90 s
t =3.05 s
t =1.3 s
2 µm
500 nm
D
500 nm
100 nm
α = 1.05
α = 0.15
MSD (µm²)
MSD (10⁻³ µm²)
Delays (s)
E
n.s
Fraction
Directed
Confined
Brownian
V1
V2
V2 C158A
V2 4A
F
Confined residence time
Brownian residence time
V1 WT
V2 WT
V2 C158A
V2 4A
Fraction
Time (s)
G
Residence time (S)
Normalized detyrosination level
n.s
****
***
Confined
Brownian
DeY level

646

Figure 3: Single molecule tracking reveals VASH briefly interacts with microtubules and catalyzes 1- 2 detyrosination events at a time.

(**A**) A Western blot showing the ectopic expression of VASH1 WT-, VASH2 WT-, V2 C158A-, and V2 4A-Halo in U2OS cells and the corresponding detyrosination levels (anti detyrosinated α-tubulin). GAPDH was used as a housekeeping protein as a loading control. The detyrosination level significantly increased upon VASH1-Halo WT or VASH2-Halo WT expression. (**B**) Schematic showing the experimental and analysis workflow. (**C**) Representative trajectories showing Brownian and confined motions, each from a single JF549 labeled VASH2-Halo molecule. The trajectories overlapped with the confocal images of microtubules labeled with Tubulin Tracker Deep red (magenta) in live U2OS cells. The duration(t) of each trajectory is indicated. (**D**) Example MSD curves showing a diffusive motion (red) and a confined motion respectively. Insets: the corresponding trajectories. The y-axes are color-coded as the trajectories and scaled to the MSD range of each motion type. The α exponent for each curve is shown. (**E**) Motion classifications for VASH1, VASH2 and VASH2 mutants. The fractions of confined, Brownian and directed motions are plotted as mean ± range (total of 4047, 2992, 2858, and 3974 trajectories pooled from 38 cells, 37 cells, 39 cells and 37 cells for VASH1, VASH2, V2 C158A, and V2 4A respectively, N= 2 experiments). Representative trajectories for each motion type are shown on the right (**F**) Double exponential fits for extracting residence time for confined or Brownian motions for each VASH variant. The insets show zoomed regions (red boxes) of the fits. (**G**) Residence time for confined and Brownian motions extracted from the long time constant of the exponential fit and corrected for photobleaching. Error bars correspond to the 95% confidence interval. The detyrosination level was calculated as a normalized value against the detyrosination level of VASH2 WT, using the western blot in (**A**). Krauskal-Willis test with Dunn's multiple comparison test was performed on all trajectories from each condition. *** $P<0.001$, **** $P<0.0001$, ns, $P> 0.05$, not significant.

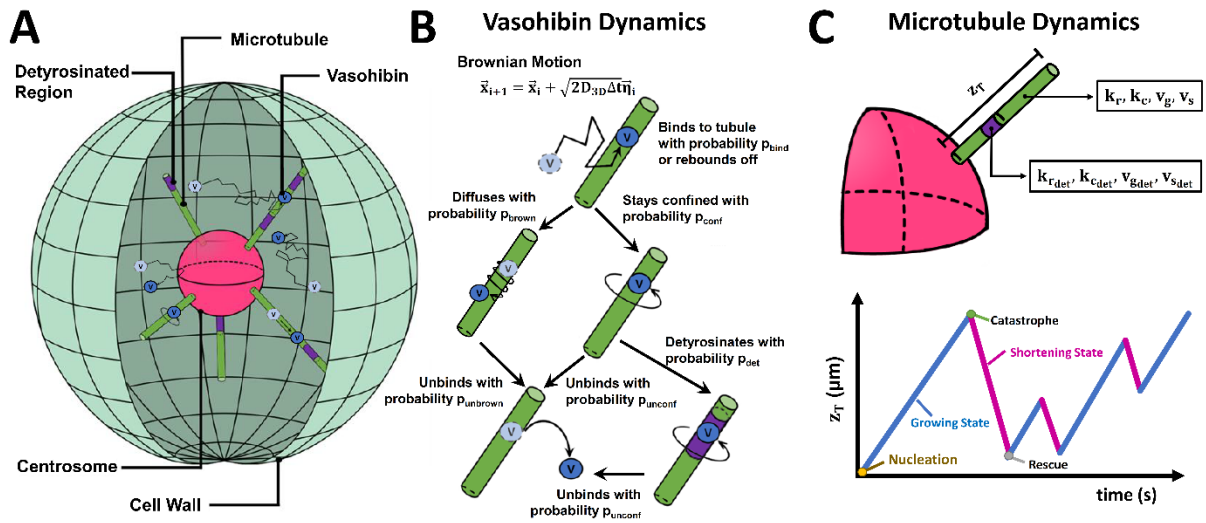

674

675 **Figure 4. Schematics of our computational model and microtubule dynamic processes. (A)**
676 Simulated system. VASH enzymes (dark blue circles) diffusing inside the cell are capable to bind
677 to existing microtubules (cylinders) and detyrosinate them (purple regions represent
678 detyrosinated areas while green regions represent tyrosinated ones), locally increasing the
679 stability of the microtubule. Light blue circles represent a previous position of a VASH enzyme in
680 the trajectory (black arrow). **(B)** Enzyme dynamics. Upon binding to a microtubule (what happens
681 with a probability p_{bind}), a diffusing enzyme either becomes confined to an α-tubulin subunit with
682 probability p_{conf}, or it performs a random walk along the surface of the microtubule with a
683 probability p_{brown}. Confined enzymes and diffusing enzymes are capable of unbinding from a
684 microtubule with probabilities p_{unconf} and $p_{unbrown}$, respectively. Confined enzymes are also capable
685 of detyrosinating the α-tubulin subunit they are bound to with probability p_{det}. **(C)** Dynamic
686 instability of a single microtubule. An α-tubulin subunit with growth and shortening rates v_g and
687 v_s, respectively, and rescue and catastrophe frequencies k_r and k_c, respectively, changes its
688 dynamic properties upon detyrosination ($v_{g_{det}}$, $v_{s_{det}}$, $k_{r_{det}}$, and $k_{c_{det}}$).

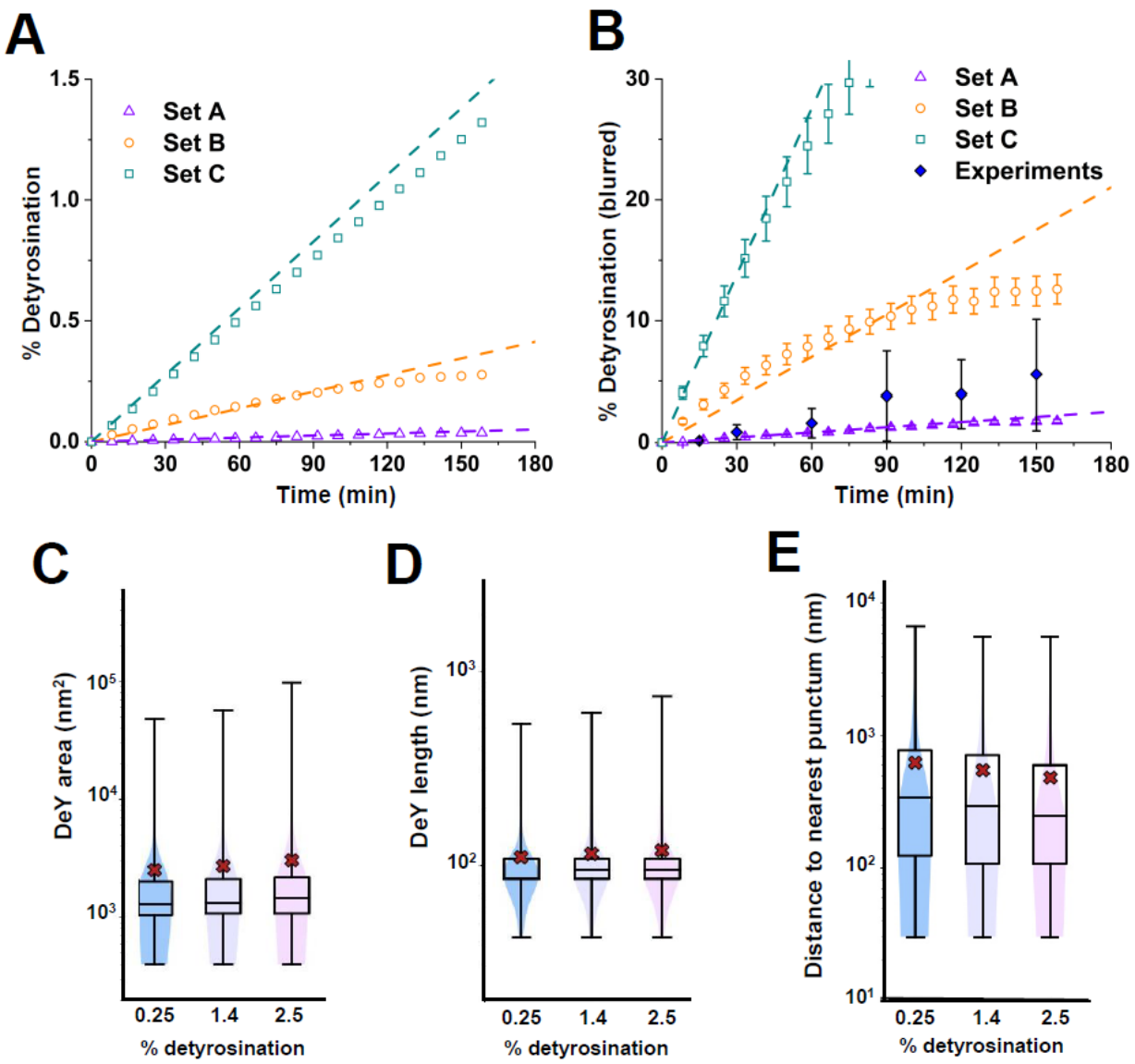

Figure 5. Detyrosination features observed in our computational model. (A) Simulated detyrosination levels (symbols) as a function of time for 250 microtubules that are highly dynamic (set A), intermediately dynamic (set B) and fully stable (set C) with 100 nM VASH. Simulated detyrosination levels are comparable to our analytical theory (dashed lines). **(B)** Comparison between experimental detyrosination levels (filled dark blue diamonds, ± SD) and simulated detyrosination levels presented in (A) (empty symbols ± SD) after blurring to experimental resolution. Puncta area **(C)**, length **(D),** and border-to-border distance between nearest puncta **(E)**, for a set of 250 highly dynamic microtubules and 100 nM VASH. Violin plots were overlaid with box and whisker plots (where the box is centered at the median value and is limited by the upper and lower quartiles) with the mean values labeled (red crosses).

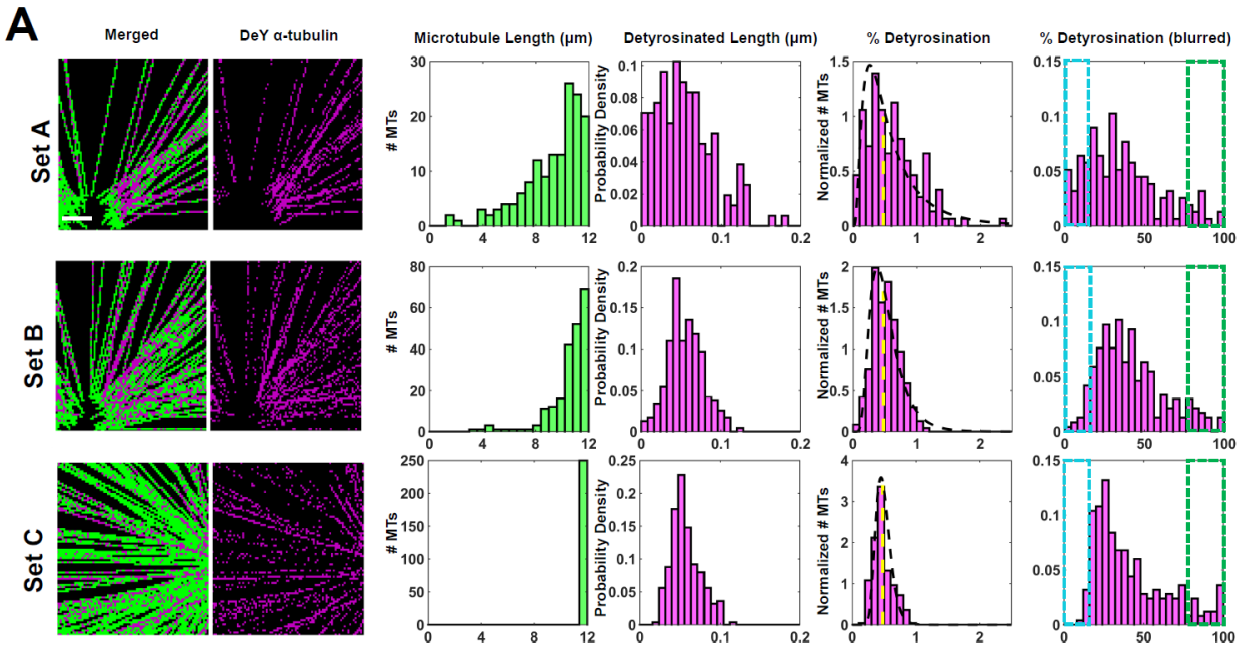

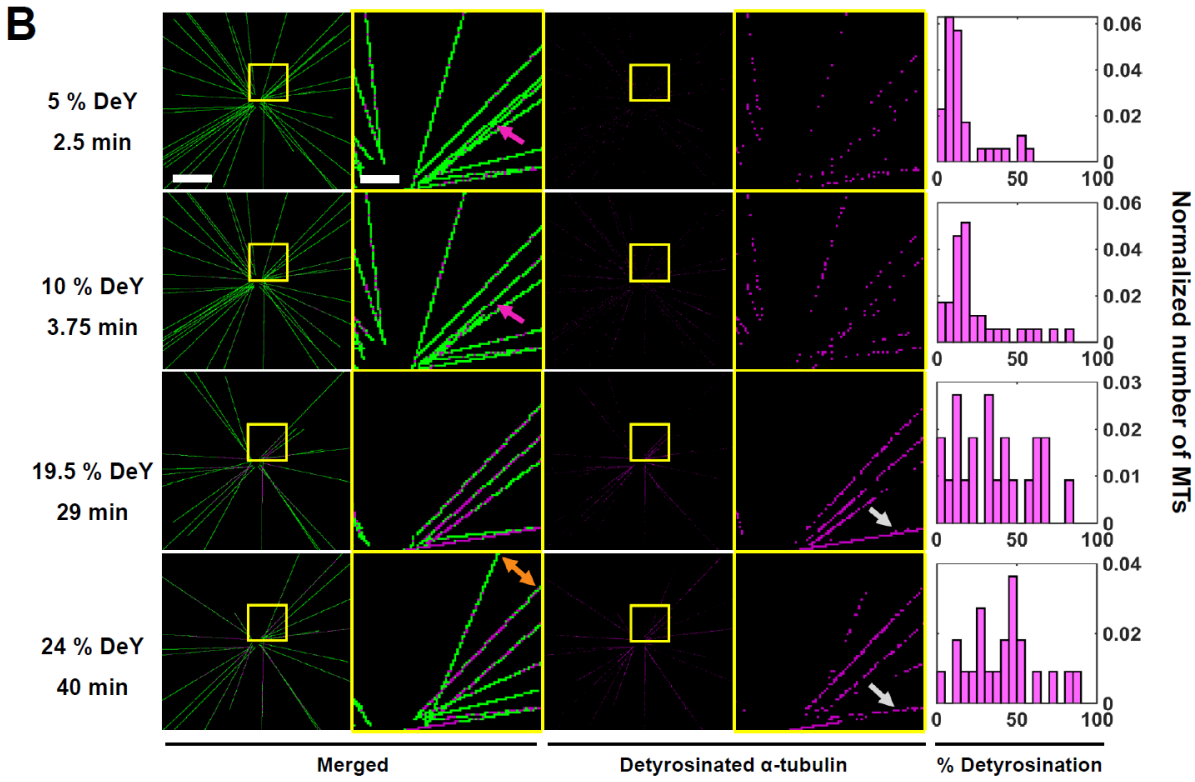

Figure 6. Due to their increased stability, highly detyrosinated microtubules co-exist with newly polymerized ones. (A) (LEFT) Representative images showing zoomed regions of highly dynamic (top, set A), intermediately dynamic (middle, set B) and fully stable (bottom, set C)

microtubules at a total detyrosination level of 23.1 ± 0.5%. Detyrosinated α-tubulin subunits are shown in magenta and β-tubulin in green. Scale bar, 500 nm. Images were blurred to experimental resolution. **(RIGHT)** Histograms of the microtubule length, detyrosinated length, and percentage of detyrosination before (left) and after (right) resolution blurring. Fully depolymerized microtubules were neglected in our histograms. Percentages of detyrosination (before blurring) were fitted by lognormal distributions (black dashed line) showing the same median values (yellow dashed lines), but different variances (σ) of 0.77 (set A), 0.47 (set B) and 0.24 (set C). Blue dashed boxes, detyrosination percentage ≤ 15 %. Green dashed boxes, detyrosination percentage ≥ 75 %. **(B) (LEFT)** Images showing a selected region of 50 highly dynamic microtubules with 1 μM VASH at specific time points and total detyrosination levels. Detyrosinated α-tubulin subunits are shown in magenta and β-tubulin in green. Scale bars: 2.5 μm, 500 nm for zoomed region (yellow open square). Images were blurred to experimental resolution. Note that a tyrosinated microtubule (magenta arrows) rapidly shortened (1.3-minute lifetime) while a highly detyrosinated one persisted (11-minute lifetime, white arrows). The orange bi-direction arrow shows an example of a highly detyrosinated microtubule positioned right next to a tyrosinated one. **(RIGHT)** Histograms of the percentage of detyrosination after resolution blurring.

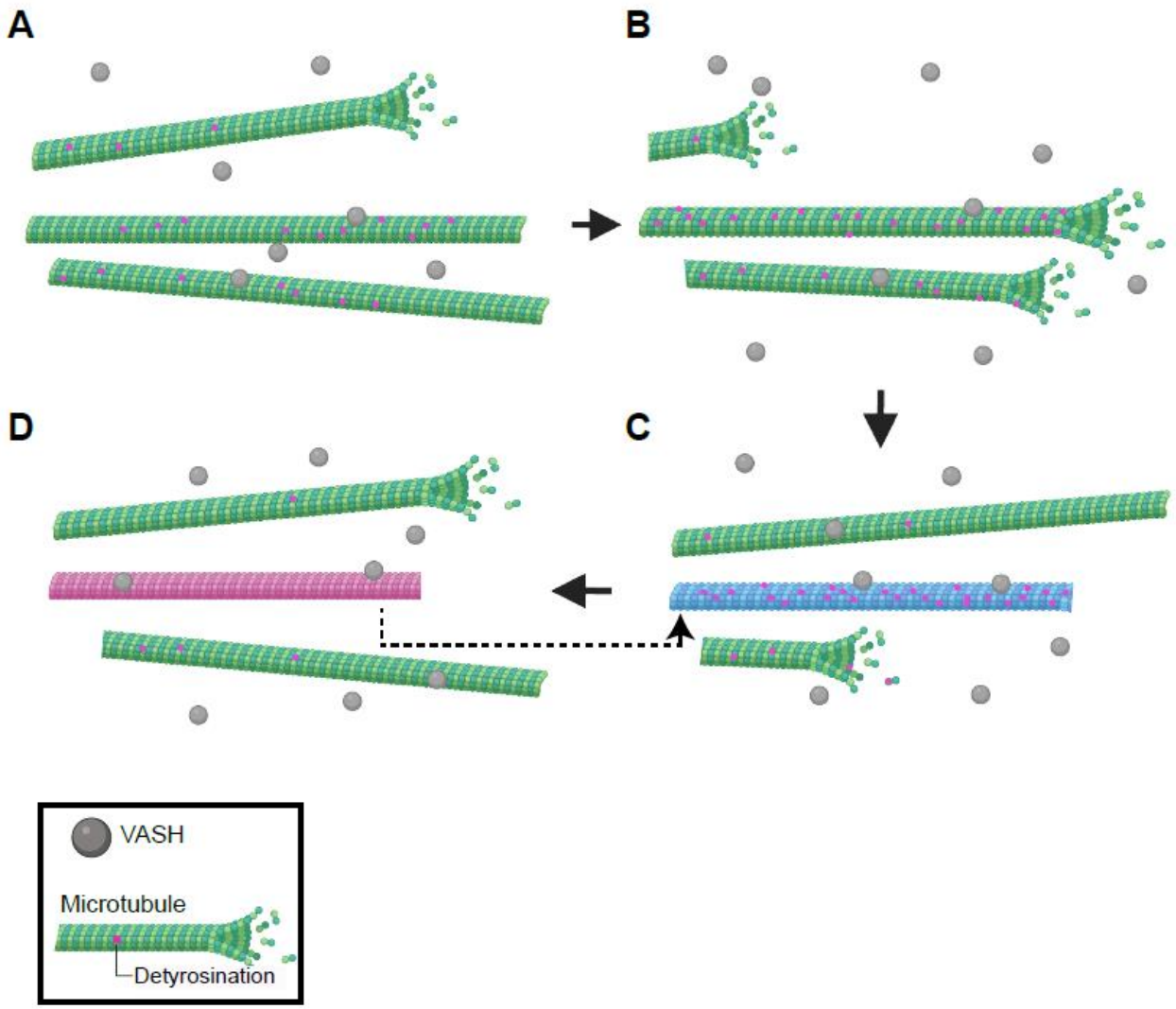

Figure 7. The feedback between microtubule stability and detyrosination.

In the cells where MAPs are present, (**A-B**) VASH stochastically acts on microtubules and by chance detyrosination level varies among different microtubules. (**C**) Over time, some microtubules become more detyrosinated and stable (shown in light blue), while the rest turnover readily and lose detyrosination. (**D**) The stability of the microtubule allows more accumulation of detyrosination events and eventually lead to much higher stability in microtubules (exemplified by a purple microtubule here). The dashed arrow indicates that the stability allows more accumulation of detyrosination, resulting in a feedback loop. It is possible that additional factors can stabilize microtubules regardless of microtubule detyrosination level, which will accelerate the evolution of stability, also leading to accumulation of more detyrosination on stable microtubules.

Tables

Table 1. Residence time and percent population of motion classes.

VASH WT and mutants	Brownian				Confined			
	Percent of total population	Residence time (s)	95% confidence interval (s)		Percent of total population	Residence time (s)	95% confidence interval (s)	
			upper limit	lower limit			upper limit	lower limit
VASH 1 WT	59.7	1.289	1.357	1.227	35.9	2.533	2.708	2.375
VASH2 WT	56.1	1.695	1.797	1.604	40.6	3.002	3.101	2.910
VASH2 C158A	56.2	1.971	2.065	1.885	40.0	2.601	2.774	2.450
VASH2 4A	58.0	1.482	1.544	1.425	37.5	2.286	2.446	2.143
VASH1 WT (washout)	51.3	1.336	1.393	1.284	45.2	1.376	1.458	1.302
VASH2 WT (washout)	53.7	1.703	1.870	1.558	42.5	2.227	2.333	2.128

All residence times shown here are corrected against photobleaching (see Methods and Figure S4).

Table 2. Common parameters used in simulations of the microtubule array. A timestep of

Parameter Name	Parameter Value
Simulation Time Step, Δt	0.01 s
Temperature, T	310 K
Cell Diameter, d_{cell}	25 µm [this work]
Centrosome Diameter, d_{center}	1 µm (Alieva and Uzbekov, 2016; Schatten, 2008)
Microtubule Diameter, d_t	25 nm (Beese et al., 1987; Ledbetter and Porter, 1963)
Enzyme Diameter, d_e	7 nm (Adamopoulos et al., 2019; Li et al., 2019; Wang et al., 2019; Zhou et al., 2019)
Nucleation Rate per Site, k_n	0.0005 s^{-1} (Cassimeris et al., 2018)
Number of Dimers in a MT n_d	1624 μm^{-1} (Cassimeris et al., 2018)
Probability of Diffusive VASH, p_{brown}	0.605 [this work]
Probability of Confined VASH, p_{conf}	0.395 [this work]
Concentration-dependent growth factor k_{on}	0.0167 $mM^{-1}s^{-1}$ (Cassimeris et al., 2018)
Ratio of Shortening Rates, $v_s/v_{s_{det}}$	1.54 (Shelden and Wadsworth, 1993)
Ratio of Catastrophe Frequencies, $k_c/k_{c_{det}}$	1.89 (Shelden and Wadsworth, 1993)
Ratio of Growth Rates, $v_g/v_{g_{det}}$	0.93 (Shelden and Wadsworth, 1993)
Ratio of Rescue Frequencies, $k_r/k_{r_{det}}$	0.95 (Shelden and Wadsworth, 1993)
Translational Diffusion Coefficient in MT, D_{1D}	0.0079 $\mu m^2/s$ [this work]
Diffusion Coefficient in Bulk, D_{3D}	1.067 $\mu m^2/s$ [this work]
Rotational Diffusion Coefficient, D_θ	0.7 rad^2/s
Binding probability p_{bind}	$1-e^{-0.48\Delta t}$ [this work]
Unbinding Probability while Diffusive, $p_{unbrown}$	$1-e^{-0.64\Delta t}$ [this work]
Unbinding Probability while Confined, p_{unconf}	$1-e^{-0.33\Delta t}$ [this work]
Detyrosination Probability, p_{det}	$1-e^{-0.74\Delta t}$ [this work]

A temporal resolution of 0.01 s was selected as an optimal value balancing total simulation time and accuracy. A rotational diffusion coefficient of 0.7 rad^2/s was selected to randomize the point of escape of the bound enzyme on the microtubule. Binding, unbinding and detyrosination probabilities (p) are related to their associated times (T) by means of $p = e^{-\Delta t/T}$.

Table 3. Parameter sets for microtubule plus-end dynamic instability.

Parameter	**Set A**	**Set B**
Initial Growth Rate v_{g_0} $(\mu m/s)$	0.142	0.192
Shortening Rate v_s $(\mu m/s)$	0.188	0.218
Catastrophe Frequency k_c (s^{-1})	0.053	0.026
Rescue Frequency k_r (s^{-1})	0.086	0.175
Tubulin Concentration (μM)	25	35

Parameters were selected based on a previous study (Cassimeris et al., 2018). For Set C, microtubules were kept at their maximum lengths throughout the simulations.

Captions for videos

Movie S1 A movie showing Brownian events (a and b in Fig 3C) from two VASH2-Halo molecules, pseudo-colored in yellow on microtubules (magenta) labeled by Tubulin Tracker. Scale bar, 1 µm. The movie is playing at 1× speed or 20 frames per second (fps).

Movie S2 A movie showing a VASH1-Halo molecule (Fig S4C) diffusing back and forth on the microtubules. Scale bar, 1 µm. The movie is playing at 1× speed or 20 fps.

Movie S3 A movie showing a prolonged diffusion from a VASH1-Halo molecule (Fig S4D) on the microtubule dense area. Scale bar, 1 µm. The movie is playing at 1× speed or 20 fps.

Movie S4 A movie showing a prolonged diffusion from a VASH2-Halo molecule (Fig S4D) on the microtubule-dense area where microtubules possibly bundle or criss-cross. Scale bar, 1 µm. The movie is playing at 1× speed or 20 fps.

Movie S5 A movie corresponding to Fig 3C, showing a VASH2-Halo (JF549) molecule is confined on Tubulin Tracker labeled microtubules (magenta). Scale bar, 1 µm. The movie is playing at 1× speed or 20 fps.

Movie S6 A movie showing a VASH1-Halo molecule is confined on a microtubule (Fig S4C). Scale bar, 1 µm. The movie is playing at 1× speed or 20 fps.

Movie S7 An example movie showing a VASH2-Halo molecule (Fig S4E) transition between Brownian and confined motions while staying on microtubules. Scale bar, 1 µm. The movie is playing at 1× speed or 20 fps.

Movie S8. An example movie showing a system of 10 microtubules (cylinders) and 10 VASH molecules (spheres) in a cell of radius 5 µm. Microtubule and enzyme diameters were increased for visualization purposes as well as the size of an α-subunit. Tyrosinated regions of the microtubules appear in green while detyrosinated regions appear in purple. Multiple parameters were modified to show faster detyrosination. As an example, one VASH molecule (black) was tracked during the simulation time and its cumulative trajectory is shown in the lower left panel.

Methods

Cell culture expression constructs.

BSC-1 or U2OS cells (BS-C-1; CCL-26; American Type Culture Collection) were routinely maintained in MEM or DMEM media (ThermoFisher) supplemented with 10% (vol/vol) FBS, 1x Glutamax, 1x Anti-Anti, 1 mM sodium pyruvate at 37 ºC with 5% CO_2. U2OS and 293T cells were cultured in DMEM media supplemented with 10% (vol/vol) FBS, 1x Glutamax, 1x Anti-Anti, 1 mM sodium pyruvate at 37 ºC with 5% CO_2. All culture media and supplements were purchased from ThermoFisher.

DNA constructs and lentivirus production of VASH and SVBP coexpression

For transient expression from plasmids, VASH1-eGFP or VASH2-eGFP (Wang et al., 2019) (kind gifts from Dr. Marie Jo-Mountin) were each co-expressed with SVBP-Myc-FLAG. Briefly, BSC-1 cells were grown to 60% confluency in 6-well plate and were co-transfected with 500 ng each of VASH-eGFP and SVBP-Myc-FLAG using Lipofectamine 2000 (ThermoFisher) following manufacturer's instructions. The media was replaced the next day and the cells were trypsinized and re-seeded onto Lab-TekII imaging chamber (Nalge Nunc, ThermoFisher). The transfected cells were imaged ~40 h post transfection.

Lentiviral expression constructs pLV- CBh-SVBP-Myc-FLAG:IRES:VASH-HALO, co-expressing SVBP and VASH WT or mutants, were commercially made (VectorBuilder, Chicago, IL and Genscript). Briefly, human SVBP-Myc-FLAG sequence were synthesized and inserted downstream of a CBh promoter and VASH coding sequences were placed downstream of an IRES element. Human VASH1 WT, VASH2 WT, VASH2 C158A, VASH2 4A coding sequences were amplified from previously published mammalian expression constructs VASH1-eGFP, VASH2-WT-eGFP, VASH2 C158A-eGFP, VASH2-4A-eGFP (Wang et al., 2019) (kind gifts from Dr. Marie Jo-Mountin).

Lentiviral particles were packaged produced by co-transfecting the expression construct pLV-CBh-SVBP-Myc-FLAG:IRES:VASH-HALO and packaging constructs (kind gifts from Dr. Ben Prosser) pCMV-VSVG, pRSV-REV, pCgpV at 3:1:1:1 ratio into 293T cells. Briefly, 45 µg of expression construct and 15 µg of each of the packaging constructs were mixed in 900 µl Opti-Mem media (ThermoFisher) and subsequently mixed with 900 µl Opti-Mem media containing 90 µl Lipofectamin2000 for 5 min. The mixture was then added to a 10 cm-plate of T293 cells at 50-

60% confluency for overnight incubation at 37 ºC. The media was replaced with fresh growth media the next day and the cells were allowed to produce virus for the next 48 hr. The media containing the packaged viral particles were collected and spun at 100 ×g for 5 min and the supernatant was passed through a 0.45 µm filter, aliquoted and stored at -80 ºC.

Nocodazole washout and immunostaining for DNA-PAINT

BSC-1 cells were grown in Lab-TekII imaging chamber. For cells treated with Nocodazole, the BSC-1 growth media containing 33 µM Nocodazole was filtered through a 0.45 µm filter and added to the cells for three hours at 37ºC. For cells that are allowed to reassemble microtubule after Nocodazole treatment (washout conditions), the cells were then washed three times with warm complete growth media and then incubated in growth media for different amount of time as indicated in the results section. For washout experiments followed by Taxol treatment, cells were quickly washed three times after Nocodazole treatment and was incubated with 2 µM Taxol or the equivalent amount of DMSO (0.04%, vol/vol, labeled untreated) for 30 min at 37ºC. To fix the cells, they were briefly (10-30 s) permeabilized by incubating with extraction buffer (80 mM PIPES-KOH pH 7.1, 1 mM EGTA, 1 mM $MgCl_2$, 0.5% Triton X-100 (vol/vol), 10% glycerol (vol/vol)) warmed to 37°C and immediately replaced by the fixation buffer (3% paraformaldehyde (PFA) and 0.1% glutaraldehyde in PBS) at 37°C for 10 min. Cells were then washed twice with PBS, incubated with fresh 0.1% NaBH4 (wt/vol) solution for 7 min and washed again three times with PBS. The fixed cells were then permeabilized for 10 minutes with 0.2% Triton X-100 (vol/vol) in PBS and blocked for one hour at 25°C using Primary Blocking Buffer (10% donkey serum (vol/vol), 0.2% Triton X-100 (vol/vol), and 0.05 mg/mL sonicated salmon sperm single stranded DNA (Stratagene, La Jolla, California) in PBS). Salmon sperm DNA was denatured at 95 ºC for 3 minutes before addition to the buffer and was included in the blocking buffer to reduce off-target binding of DNA-PAINT secondary antibodies and imagers to nuclear DNA. Cells were then incubated with primary antibodies at 1:100 unless otherwise indicated in the figure legends in Primary Blocking Buffer, for one hour at 25°C or at 4ºC overnight. Following primary antibody incubation, cells were washed once with PBS, followed by three five-minute washes with Wash Buffer (Massive Photonics, Gräfelfing Germany). Cells were then incubated with secondary antibodies (anti-mouse and anti-rabbit DNA-PAINT secondary antibodies, Massive Photonics) at 1:100 dilution in Antibody Incubation Buffer (Massive Photonics). Cells were then washed once with PBS briefly, followed by three ten-minute washes with 1X Wash buffer (Massive Photonics).

Finally, cells were washed once for five minutes with PBS, and stored in fresh PBS at 4ºC until imaging.

DNA-PAINT Imaging

DNA-PAINT images were acquired using a Nanoimager (ONI, Oxford, UK) equipped with 405-, 488-, 561- and 640-nm lasers, 498-551- and 576-620-nm band-pass filters in channel 1, 666-705-nm band-pass filters in channel 2, a 100 x 1.45 NA oil immersion objective (Olympus), and a Hamamatsu Flash 4 V3 sCMOS camera. All images were acquired with 100 ms exposure at 30°C using HILO illumination (Tokunaga et al., 2008). Before imaging, imager DNA oligos (Massive Photonics) complementary to the conjugated secondary antibody docking oligos were diluted in Imaging Buffer (Massive Photonics) and added to imaging wells. To perform two-color imaging, for beta tubulin and acetylated tubulin, 0.25 nM of Imager-1 Cy3B or Imager-1 ATTO655 was used, and 5,000 total frames were acquired. This was sufficient to capture a continuous image of microtubules, allowing for their use as a location reference for detyrosination signal in subsequent analysis. For detyrosinated tubulin, 0.5 nM of Imager-2 Cy3B or Imager-2 ATTO655 was used, and 10,000 total frames were acquired. The laser program (Oxford Nanoimaging) alternates acquisitions between the two channels (100 frames of beta or acetylated tubulin followed by 200 frames of the detyrosinated tubulin) until the total 15,000 frames were recorded. For single-color imaging of acetylated microtubules for Nocodazole washout experiments, 0.5 nM of Imager-1 Cy3B or Imager-1 ATTO655 was used were used and 10,000 total frames were acquired. Images were then drift-corrected and filtered using the NimOS localization software (ONI) with filtering parameters as follows: X/Y localization precision (0-30 nm), Sigma X/Sigma Y (10-150 nm). All images regardless of experimental condition were filtered using these same parameters.

Western blot

U2OS cells were grown to 50-60% confluency in 6-well plate and incubated with 400 µl lentivirus carrying the appropriate expression cassettes in a total volume of 1 mL culture media containing final concentration of Polybrene at 10 µg/mL per well overnight. The lentivirus containing media was removed the next day and the cells were trypsinized and seeded onto new wells to continue growth for another day. The cells were trypsinized and pelleted 40 hr post viral transduction and the pellets were solubilized with 1x LDS Sample buffer (ThermoFisher) supplemented with 1x

Sample Reducing agent (ThermoFisher) and boiled for 7 min at 98 ºC. The samples were resolved on a 10% Bis-Tris gel (Novex) and transferred to nitrocellulose blot. The blot was incubated with Odysee TBS blocking buffer (Licor) for 1 hr at 25 ºC followed by incubation with primary antibodies, anti-Halo (1:1000, mouse, Promega), anti-Myc (1:100, Rabbit, Proteintech), anti-detyrosinated α-tubulin (1:1000, Rabbit, Abcam) and anti-GAPDH (1:2000, mouse, Proteintech) overnight, and the blot washed three times with 1xTBST (ThermoFisher) and secondary antibodies (680-anti mouse, 800-anti rabbit) at 1:10000 for 1 hr at 25 ºC followed by three washes of TBST. The Western blot was imaged on Licor imaging system and the signal was quantified using the Licor imaging studio software. Detyrosination level was normalized to GAPDH level. To compare the exogenous level of detyrosination due to the ectopic expression of VASH-Halo, detyrosination was first quantified and normalized to GAPDH, and the basal level of detyrosination in un-transduced U2OS was then subtracted from all conditions that express VASH-Halo. The subtracted detyrosination level was then normalized to VASH2-Halo level. Detyrosination level due to VASH2 WT expression was arbitrarily set to one and all other conditions were described as a relative detyrosination level normalized to VASH2 WT (Figure 3A and 3G).

Single molecule imaging of VASH-Halo

U2OS cells were grown to 50-60% confluency in a 12-well plate and transduced with 100 ul of lentivirus carrying the appropriate expression cassettes in a total volume of 400 ul culture media containing final concentration of Polybrene at 10 ug/mL per well overnight. The lentivirus containing media was removed the next day and the cells were trypsinized and seeded onto Lab-TekII imaging chamber and allowed to grow overnight. On the day of imaging (~40 hr post viral transduction), cells were incubated with 20 nM of Halo ligand JF549 (Promega) in growth media for 15 min at 37 °C followed by three washes of warm growth media. Then the cells were labeled with Tubulin Tracker Deep red (ThermoFisher) following the manufacturer's instruction. Briefly, the cells were incubated with 1× Tubulin tracker (1 µM) in growth media for 30 min at 37 °C. The cells were then washed three times with imaging media (L-15 lebovitz media (ThermoFisher) supplemented with 10% (vol/vol) FBS, 1× Glutamax, 1× Anti-Anti, 10 mM HEPES, 770 µg/mL Probenecid) and left in imaging media for imaging for no more than two hours. For single molecule imaging post Nocodazole washout, the cells were grown, infected with lentivirus and seed similarly as aforementioned. Prior to imaging, the cells were treated with 33 µM Nocodazole (0.45 µm membrane filtered) for 3 h at 37 ºC. The cells were then quickly washed three times with

complete DMEM culture media and incubated with Tubulin Tracker Deep red for 30 min at 37 ºC, followed by similar wash and imaging steps with imaging media.

Single molecules and microtubules are visualized and recorded using an Nanoimager (ONI) warmed to 30 °C. For each recording, the microtubule confocal image was first captured in the confocal mode on Nanoimager with 500 ms exposure per slice using 640 nm laser at 65%-75% power for 10 consecutive slices. Immediately after, VASH-Halo was imaged in the widefield mode with HILO illumination using 560 nm laser at 15% laser power and the images were acquired at 50 ms exposure for 2500 frames, or a total of 125 s.

Data Analysis

DNA PAINT

DNA PAINT images were analyzed using a custom-written Matlab code modified from a previous version (Mohan et al., 2019). Drift-corrected and sigma filtered (Nanoimager software, Oxford Nanoimaging) localizations were Voronoi segmented and clustered based on consistent Voronoi area threshold across all conditions (616.005 nm^2 for detyrosinated tubulin and 5475.6 nm^2 for beta/acetylated tubulin, each with minimum of 5 localizations per cluster/puncta). The large Voronoi area threshold for beta/acetylated tubulin is to ensure microtubules were clustered as a continuous network for localization references. Detyrosinated puncta that are denser (in localization per Voronoi area) than two standard-deviation from the mean were excluded from the detyrosinated images as non-specific background noise. Microtubule network clusters with Voronoi area less than 41067 nm^2 were discarded as background noise. Detyrosinated microtubules were then overlaid with the reference microtubules and the detyrosinated puncta with ≥40% of their area overlapped with microtubules were considered colocalized with microtubules. The microtubule-colocalized detyrosinated puncta areas were calculated from the bounding puncta areas contoured by a Matlab built-in alphaShape function. Colocalized detyrosinated puncta from all experiments were filtered against a minimum area of 400 nm^2 (area calculated from alphaShape objects), which is considered the resolution limit for DNA-PAINT. The lengths of the detyrosinated puncta were defined as the longest axes from principle component analysis (PCA) rotation of the puncta. The distance to the nearest punctum was the smallest Euclidean distance between borders of puncta.

To calculate the contribution of background noise to all detyrosinated signal, the puncta that have density (number of localizations per Voronoi area) larger than two standard-deviation away from the mean were first excluded. Then detyrosinated image was flipped horizontally and then vertically with respect to the microtubule reference image. The fraction of false positive co-localization was determined as the sum of the area of the flipped detyrosinated α-tubulin image co-localized with the β-tubulin image divided by the sum of the area of the original detyrosinated α-tubulin image co-localized with the β-tubulin image.

To calculate the number of detyrosination site per puncta, we used the detyrosination image obtained by staining with anti detyrosinated α-tubulin antibody at 1:2500 dilution as the single detyrosination calibration. The detyrosinated images (Figure 2D, 2E and Figure S2) were post-processed and colocalized with acetylated microtubules same as described above. The number of localizations per colocalized detyrosinated punctum was plotted as a histogram distribution and fitted to a lognormal function:

$$pdf = \frac{1}{x\sigma\sqrt{2\pi}} e^{\frac{-(\ln(x)-\mu)^2}{2\sigma^2}}$$

The x is the number of localizations. The mean (μ) and variance (σ) were obtained from the fit.

The 2-, 3-, 4-, 5-detyrosination site calibration functions were obtained by linear convolution of the single detyrosination site calibration function from the lognormal fit using a custom-written Matlab code. The number of localizations per colocalized detyrosinated puncta from images at 30 min, 60 min and 90 min post Nocodazole washout were plotted as histograms and were fitted to the combination of calibration functions with weights w_1, w_2, w_3, w_4, w_5 corresponding to the proportions of 1, 2, 3, 4, 5 detyrosination sites. The 3+ sites in the graph of 90 min post Nocodazole washout (Figure 2F) corresponds to the combined weight of w_3, w_4 and w_5.

The total experimental detyrosination level (Figure 5B) is the calculated as the area sum of the detyrosinated clusters were divided by the area sum of the total microtubules for each cell.

Single molecule tracking and analysis

Single molecules of VASH-Halo were tracked with ImageJ (NIH) plugin Trackmate (Tinevez et al., 2017). Spots were detected using the LoG detector with 0.8 µm diameter threshold and subpixel localization and were subsequently linked as trajectories using Simple Lap Tracker with 0.6 µm maximum linking distance and maximum 1 frame gap. The linked trajectories were

exported as XML files and analyzed using a custom-written MATLAB code. Briefly, Mean square displacement (MSD) of each trajectory is fitted to the power law function as below (Gómez-García et al., 2021):

$$MSD = 4Dt^{\alpha}$$

The D is the diffusion coefficient, t is the time lag between time points of the trajectories, and the first 25% of time lag of the MSD was fitted to extract the α exponent. Only trajectories ≥ 10 frames (0.5 s) were analyzed. Trajectories were then overlaid with the corresponding microtubule confocal image which were binarized using the local thresholding function in ImageJ. Trajectories with less than 20% of their segments overlapped with microtubules were considered not on the microtubule network. The 20% overlap threshold accounts for certain degree of microtubule fluctuations during the 125 s imaging time at 30 ºC (Fig S4A). All trajectories were then manually inspected against the original confocal images to correct any mis-categorization. The motions were then classified based on the value of the α exponent as follows, $\alpha \leq 0.8$, confined; $0.8 < \alpha < 1.5$, Brownian; $\alpha \geq 1.5$, directed, and trajectories in all categories are filtered with coefficient of determination $R^2 \geq 0.8$.

Residence time calculation

The residence time was calculated for Brownian and confined categories separately. In each category, all trajectories were pooled and plotted as survival fraction of molecules using 1-Cumulative Distribution Function of the trajectory duration. We then fit the survival curve with a two exponential decay function as follows ((Ball et al., 2016; Chen et al., 2014; Mazza et al., 2012).

$$F(t) = fe^{-k_{fast}(t-0.5)} + (1-f)e^{-k_{slow}(t-0.5)}$$

The f is the fraction of short-lived trajectories and the (1-f) is the fraction of long-lived trajectories. We used t - 0.5 instead of t because the minimum trajectory duration is 0.5 s (10 frames) as previously mentioned. The residence time is the fitted slow lifetime (long-lived component). The dissociation rate constant (k_{off}) used in the simulation is extracted from the confined residence time from VASH2-Halo.

Correction for photobleaching

The photobleaching rate constant ($k_{photobleaching}$) was calculated by fitting a single exponential decay function with an offset to the number of detected spots per frame over time.

The corrected slow dissociate rate constant ($k_{corrected}$) is calculated as below:

$$k_{corrected} = k_{slow(measured)} - k_{hotobleaching}$$

The residence time was corrected based on the corrected k_{slow} (slow dissociation rate constant). The statistics and fits for residence time and correction for photobleaching were performed using Graphpad Prism software.

Computational Model

Monte Carlo model of Microtubule Dynamics

A Monte Carlo model was implemented to simulate an array of dynamic microtubules (Cassimeris et al., 2018). Microtubules grow and shrink by exchanging polymeric subunits with a soluble pool of tubulin, found in cells at a total concentration $\mathrm{C_T}$. All microtubules are nucleated from the boundary of a sphere of diameter $\mathrm{d_{center}}$ located in the center of a spherical shell of diameter $\mathrm{d_{cell}}$, representing the centrosome and outer boundary of our cell, respectively. The number of nucleation sites is set as $\mathrm{N_T}$, which also sets the maximum number of microtubules. At time $\mathrm{t} = 0$, all microtubules are put in growth state, and they grow at a rate $\mathrm{v_{g_o}}$ for a time $\Delta\mathrm{t}$. After this initial step, each microtubule can either stay in growing state or a catastrophe event can happen, putting the microtubule in shortening state. Catastrophe events (growing to shortening transitions) happen to a growing microtubule with a frequency $\mathrm{k_c}$. For those microtubules that stay in growing state, the growth rate is considered as dependent on the free tubulin concentration after this initial step, $\mathrm{v_g} = \mathrm{k_{on}C}$. As one micrometer of microtubule is made up of $1\ \mu\mathrm{m} \cdot \mathrm{n_d}$ dimers, $\mathrm{C_T} = \mathrm{C} + \left(\mathrm{n_d} \sum_{\mathrm{i=1}}^{\mathrm{N}} \mathrm{L_i}\right)/(\mathrm{N_A V_{cell}})$, where $\mathrm{L_i}$ is the length of microtubule i, $\mathrm{V_{cell}}$ is the cell volume and $\mathrm{N_A}$ is the Avogadro number. microtubules keep growing until they either undergo a catastrophe or reach the cell boundary, where they immediately transition to shortening state. Shortening microtubules reduce their lengths at a rate $\mathrm{v_s}$ independent of tubulin concentration, and the shortening of microtubule i increases the free tubulin concentration by $(\mathrm{n_d}\Delta\mathrm{L_i})/(\mathrm{N_A V_{cell}})$, where $\Delta\mathrm{L_i}$ is the change in length of microtubule i. During its shortening state, a microtubule can either reach the centrosome of the cell or undergo a rescue event (shortening to growing transition). A microtubule which reaches the centrosome will completely depolymerize, and a new microtubule can be

nucleated from this empty site with a frequency k_n. Rescue events happen with a frequency k_r and they put a microtubule in growth state. All microtubules grow and shorten linearly, and their nucleation sites and directions of growth are selected at random during the first nucleation event. microtubules are modeled as cylinders of diameter d_t, and their positions are selected to avoid intersections between microtubules or between microtubules and the centrosome. Two different sets of parameters for microtubule dynamics were employed in our simulations. Set B generates overly stable microtubules, which grow to long lengths and rarely depolymerize. Set A generates more dynamic microtubules, with lower tubulin concentrations, lower rescue frequencies and higher catastrophe frequencies, which better agree with experimental data (Cassimeris et al., 2018). Common parameters used to simulate microtubule arrays are shown in Table 2. Parameters associated to each of our microtubule sets are shown in Table 3. Schematics of our system and microtubule dynamic processes are shown in Figure 4. Comparison between the dynamics of sets A and set B are shown in Figure S8.

Reactive Brownian Dynamics

When a VASH enzyme is introduced in a cell containing an array of microtubules, the enzyme diffuses in the cell until it binds to one of the microtubules, which it can detyrosinate locally. VASH enzymes are modeled as spheres of diameter d_e which undergo 3D Brownian motion in the cell with a diffusion coefficient D_{3D}. As enzymes cannot leave the cell, enter the centrosome, or traverse microtubules, special considerations must be taken to avoid these events. After a move is made at each time step Δt, the new location of the enzyme is checked to make sure that it follows these restrictions. If it does not, the location is rejected, and the enzyme is moved to a new location before the start of the next time step. When the enzyme either leaves the cell or enters the centrosome, this new location is determined by calculating the distance between the rejected location and the boundary in question and moving the enzyme along the vector going from the rejected location to the previous position with a magnitude equal to the measured distance. When the enzyme traverses a microtubule, it either binds to the tubule at the first intersection of the line defined by the previous and present positions and the microtubule with a probability p_{bind}, or it instantly rebounds from the tubule with a probability $1 - p_{bind}$. In such case, the rebound is modeled akin to a rebound from the cell wall. A number N_E of enzymes is randomly introduced in the system, and enzyme-enzyme interactions are neglected to keep the system computationally inexpensive.

When an enzyme successfully binds to a microtubule, it can slide along it in a diffusive ("Brownian") manner, modeled by adding together a 1D Brownian motion with diffusion coefficient

D_{1D} along the axis of the microtubule and a 1D rotational Brownian motion with diffusion coefficient D_θ along this same axis. Otherwise, it can stay confined in a certain tubulin subunit of length δ, modeled by a pure 1D rotational Brownian motion with diffusion coefficient D_θ along the axis of the microtubule. Directed modes of motion are neglected in this model. A molecule that binds to a microtubule can be found in Brownian (diffusive) mode with probability $\mathrm{p_{brown}}$, or in confined mode with probability $\mathrm{p_{conf}} = 1 - \mathrm{p_{brown}}$. As a Brownian enzyme rarely becomes confined and vice versa, we will assume enzymes do not change modes during their bound state. The motion of Brownian enzymes can lead to escapes from the cell or into the centrosome. Hence, previously described boundary considerations are also applicable in this case. Brownian enzymes rebound at the end of the microtubules as well.

Another relevant process that enzymes may undergo after binding to a microtubule is unbinding, which can happen either randomly or as the result of the depolymerization of the subunit the enzyme is currently positioned in. The probability of unbinding differs based on the state of the enzyme. If the enzyme was diffusing along the microtubule, the probability of unbinding is given by $\mathrm{p_{unbrown}}$. On the other hand, if the enzyme was confined, the probability of unbinding is given by $\mathrm{p_{unconf}}$. After depolymerization, any enzyme located on a depolymerized subunit unbinds immediately. When an enzyme unbinds, it returns to its 3D Brownian motion regime, where it is again able to freely diffuse in all directions throughout the cell. The ejection of the enzyme from the microtubule is done along random direction, selected to avoid traversing the microtubule, over the same distance the enzyme would move were it freely diffusing in 3D.

Modeling Detyrosination

To detyrosinate a microtubule subunit, an enzyme must stay bound to it for a time $t_{det} \sim 1.35$ s based on its previously measured catalytic rate K_{cat} (Li et al., 2019). Molecules exhibiting confined motion stay bound to a subunit for an average time $\mathrm{t_{conf}} \sim 3.03$ s, while those exhibiting Brownian motion stay bound to a microtubule for an average time $\mathrm{t_{brown}} \sim 1.56\ \mathrm{s}$. During these $\sim 1.56\ \mathrm{s}$, diffusing molecules move through many microtubule subunits very rapidly, staying on a particular one only for a time $\sim (\delta_t^2/D_{1D})^{1/\alpha}$ before moving to the next one, with δ_t the length of the α-tubulin subunit (~ 4 nm) and $\mathrm{D_{1D}}$ the coefficient of Brownian motion (MSD(t) = $D_{1D}t^{\alpha}$). This time is much smaller than $\mathrm{t_{det}}$. Hence, we will assume only confined enzymes are capable of detyrosinating the subunit they are bound to, what they do with a probability $p_{det} = 1 - e^{-\Delta t/t_{det}}$. Note that, as $t_{conf} > t_{det}$, most confined enzymes are effectively capable of detyrosinating the subunit they are located at.

Once a subunit is detyrosinated, the dynamic properties associated to that subunit are modified, impacting the overall trends observed. This is modeled by changing the local frequencies and rates of a certain subunit k_r, k_c, v_g, v_s into $k_{r_{det}}$, $k_{c_{det}}$, $v_{g_{det}}$, $v_{s_{det}}$. The most significant changes involve the microtubule shortening properties. When a subunit is detyrosinated, catastrophe frequency and shortening rates decrease while growth parameters remain relatively invariant. As catastrophe events occur much less frequently, and shortening rates are significantly reduced, detyrosination leads to increased microtubule stability (see **Figure S8**).

Due to the polymeric nature of the microtubules, microtubule dynamics are dictated by the state of the subunit at the end of the microtubule, meaning that when a microtubule is in shortening state, its dynamics may change from subunit to subunit as they are removed (depolymerize). Subunits that have been detyrosinated cannot return to a tyrosinated state while they are polymerized in a microtubule (Szyk et al., 2011). The only way in which these subunits may return to the tyrosinated state is if they are depolymerized. Newly polymerized subunits are exclusively tyrosinated, meaning that after regrowth the previously detyrosinated subunit will now be in a tyrosinated state. For simplicity, we will consider each cylindrical microtubule to be split into uniformly distributed subunits bound by equidistant planes parallel to the cylinder's base. As each micrometer of a microtubule has $1\ \mu\mathrm{m} * \mathrm{n_d}$ subunits, our subunits will have a height of $\delta = 1 / n_d$, or approximately 0.6 nm. This length is much smaller than the size of an α-tubulin subunit. However, we assume the detyrosination level will be well modeled using this treatment, as the number of subunits per micrometer remains constant.

Analytical Model for the Detyrosination Level of a Microtubule Array

As detyrosination mostly takes place by the action of confined enzymes, the detyrosination level of a microtubule array will be tightly coupled to the number of binding events leading to confined motion. If each of these events culminates in the detyrosination of a different microtubule subunit, and if our system does not add or remove subunits nor returns detyrosinated subunits to their tyrosinated state (as in the case of fully stable microtubules), the total detyrosination level of our microtubule array at a time t, det(t), will be given by $N_{conf}(t) / N_{sub}$, where $N_{conf}(t)$ is the cumulative number of binding events leading to confined motions during that time and N_{sub} is the number of available subunits in the microtubule array. N_{sub} can be approximated by $\mathrm{N_{sub}} \sim \mathrm{N_T L_T}/\delta$, where N_T is the total number of microtubules and L_T is the average microtubule length, equal to $[d_{cell} - d_{center}]/2$ for fully stable arrays. Comparisons between this expression and simulations for fully stable microtubules are shown in Figure S10A (green). While our first hypothesis will remain valid if $\mathrm{N_{conf}(t)} \ll \mathrm{N_{sub}}$, our second hypothesis will not be valid for dynamic microtubules,

as both the detyrosination level and the number of available subunits may be modified at any given time by the shortening-growing cycles of the microtubules' plus-ends. Furthermore, N_{sub} will not be constant during the simulated time. We will implicitly account for these deviations from our theory by introducing a correction factor Ω, which depends only on the intrinsic dynamics of the microtubule array, $\det(\mathrm{t}) \sim N_{conf}(t)\Omega/N_{sub}$. Also, for simplicity, we will consider N_{sub} as the average number of available subunits of an identical microtubule array in absence of VASH enzymes. The correction factor Ω is taken as a fitting constant introduced to capture the tyrosination recovery observed in highly dynamic (Ω ~ 0.015) and intermediately dynamic microtubules (Ω ~ 0.195). Our theory predicts Ω ~ 1 for fully stable microtubules, however, better agreement was found with Ω ~ 0.85. Comparisons between our expression for the detyrosination level and simulations for dynamic microtubules are shown in Figure S10A (orange and purple)**.** We expect our previously derived expressions to be inaccurate for large times, as microtubules gain stability with detyrosination and it becomes increasingly rare for enzymes to visit available subunits without repetition. However, we believe they will be accurate enough for the times experimentally reported, where the percentage of detyrosination has been shown to be of only a few percent.

To estimate the cumulative number of binding events leading to confined motion N_{conf} (t), we decompose the simulation time into the time an average enzyme stays diffusing in the bulk, t_{3D}, and the time it stays bound to any microtubule, $t_{bound} \sim (N_{conf}/N_E)t_{conf} + (N_{brown}/N_E)t_{brown} + (N_{dir}/N_E)t_{dir}$. In this expression, N_E is the number of enzymes, N_{brown}, N_{conf} and N_{dir} are the cumulative number of binding events leading to Brownian, confined, and directed motions, respectively, and t_{brown}, t_{brown} and t_{dir} are the residence times of individual binding events associated to these motions. Note we include N_{dir} in our derivations for the sake of completeness, as our computational model does not consider directed motion. Defining t_{diff} as the average time a molecule spends diffusing in the bulk between two binding events, $t_{3D} \sim t_{diff}\left[(N_{conf}/N_E) + (N_{brown}/N_E) + (N_{dir}/N_E)\right]$. Finally, as the total simulation time $t = t_{3D} + t_{bound}$, and N_{conf} / p_{conf} = N_{brown} / p_{brown} = N_{dir} / p_{dir} with p_{brown}, p_{conf} and p_{dir} the probabilities that a binding event will lead to Brownian, confined, or directed motion, respectively, the cumulative number of binding events leading to confined motion may be estimated through

$$N_{conf} \approx N_E t\left(\frac{p_{conf}}{t_{diff} + t_{conf}p_{conf} + t_{brown}p_{brown} + t_{dir}p_{dir}}\right). \quad (2)$$

This expression was tested against simulations for parameters provided in Supplementary Table 2, showing great agreement along multiple scales (see Figure S10B). Numerical estimates of p_{conf}, p_{brown}, t_{diff} and t_{conf} can be obtained from our experiments (see Table 2). The number of enzymes and the mean time between individual binding events for an individual molecule remain unknown. However, the equations derived here are general enough to provide fundamental understanding on how detyrosination evolves in microtubule arrays, not only useful to better understand the dynamics of living cells but also with potential applications in diverse areas of nanotechnology such as synthetic biology (Fredy et al., 2017; Zhan et al., 2022).

The average time between binding events for an individual molecule, t_{diff}, depends on the geometrical structure of the microtubule array and cell (Bénichou et al., 2011; Chevalier et al., 2010), the dynamic behavior of the diffusing molecule (Bressloff, 2020; Mutothya and Xu, 2021; Slutsky and Mirny, 2004), and the probability with which the molecule binds to a microtubule. For a Brownian walker that freely diffuses in an infinite 3D lattice with a diffusion coefficient D_{3D} and that immediately binds to traps uniformly located along this lattice at a distance d, the average time between binding events scales as $t_{diff} \sim d^2/6D$ (Spichal and Fabre, 2017). If binding happens with a probability p_{bind}, this time will be roughly increased by the inverse of such probability (Sensale et al., 2022). In a complex system containing random or fractal obstacles and traps, as in the case of the branched arrays of microtubules living in a cell, the distance between binding sites is non-uniform and the dynamics of the diffusing particles are convoluted by the diverse interactions of the molecules with the different cellular entities, leading to anomalous behaviors and non-linear relations between binding time and the parameters of the system. For N_T linear microtubules nucleated from the boundary of a sphere located in the center of a spherical shell, representing the centrosome and outer boundary of our cell, and N_E freely diffusing Brownian walkers which bounce after hitting either the centrosome or the cell boundary and are capable to either bind or rebound after hitting a microtubule with probabilities of p_{bind} and 1- p_{bind}, respectively, we empirically observe the average time between binding events scales as $t_{diff} \sim A/N_T^{2/3} p_{bind}$, where A is a coefficient which consolidates the effects of diffusion (decreases with increasing diffusion coefficients), molecule sizes (decreases with microtubule and enzyme diameters) and intrinsic microtubule dynamics (decreases with microtubule stability, as more stable microtubules allocate a larger number of binding sites, Figure S10D).

Mimicking Experimental Resolution

Measuring the detyrosination level of each microtubule in our simulations is straight-forward, as we can keep track of the plus-end position of each microtubule and the tyrosination state of its subunits. The ratio between total detyrosinated length of a microtubule and its full length provides its detyrosination level. Averaging this ratio among all microtubules provides the total detyrosination level of our system. To compare this value to experiments, we must reduce the resolution of the system to that of the imaging method. For this task, we first reduced the dimensionality of our 3D system to 2D by projecting the microtubule array into the x-y, y-z and x-z planes. After this step, each microtubule subunit (whether detyrosinated or not) was randomized by localizing it a random number of times selected from the log-normal distribution of the number of localizations from single detyrosinated subunit (Figure 2E) with μ= 2.7952 and standard deviation σ=0.64166 (values derived from our calibration experiment for a single detyrosinated subunit), over a random direction and a distance selected from a Gaussian distribution of width 30 nm. For a microscope resolution of 30 nm x 30 nm, jittered locations were blurred by discretizing the cell with a square mesh of 30 nm x 30 nm elements, and the presence of microtubules and detyrosinated sites were stored in binary arrays. Detyrosination levels were averaged over the three projected planes. For a system of sparse microtubules, where subunits associated with two different microtubules are unlikely to coexist in a single pixel, each pixel may include up to $\sim 30/0.6 = 50$ subunits. A detyrosinated pixel will then be equivalent to $\sim$ 50 detyrosinated sites, increasing the detyrosination level of a microtubule array. Denser microtubule arrays may include more subunits per pixel. However, for our specific geometry and (relatively) low detyrosination levels (< 20%), the detyrosination level of our blurred microtubule arrays was well related to the "true" detyrosination level by multiplying it by a constant $\chi \sim 50$, as shown in Figure S10C.

Introduction of the blurring parameter χ allows us to write the detyrosination level of a microtubule array explicitly,

$$det(t) \approx \frac{\Omega \chi N_E}{N_T L_T n_d} \left[\frac{p_{conf}}{t_{diff} + t_{conf} p_{conf} + t_{brown} p_{brown} + t_{dir} p_{dir}} \right] t. \quad (1)$$

Note this equation was derived for fully stable microtubules at low detyrosination levels, and it was empirically corrected for dynamic microtubules by the introduction of a correction factor Ω. Comparisons between this theory and simulations are shown in **Figure 5 B-C**, where we can observe that the linearity of our theory with time overestimates the detyrosination levels when large, as the ratio between detyrosinated puncta and detyrosinated subunits increases ($\chi \ll 50$; see **Figure 7**).

Acknowledgments

We thank Dr. Elena Sorokina, Dr. Melina Gyparaki for technical assistance, and we are grateful for reagents provided by Dr. Marie Jo-Mountin (University Grenoble Alpes) and Dr. Ben Prosser (University of Pennsylvania). We also thank Dr. Ekaterina Grishchuk, Dr. Michael Ostap, Dr. Ben Prosser, and Dr. Dimitrios Vavlylonis for critically reading the manuscript. This work is funded by R01 GM133842 (to M.L.), RM1 GM136511 (to M.L.) and CMMI-1548571 (to M.L.). Computational simulations used services provided by the OSG Consortium (Pordes et al., 2007; Sfiligoi et al., 2009), supported by the National Science Foundation awards #2030508 and #1836650, and by the Texas Advanced Computing Center (TACC) at The University of Texas at Austin.

References

Adamopoulos, A., Landskron, L., Heidebrecht, T., Tsakou, F., Bleijerveld, O.B., Altelaar, M., Nieuwenhuis, J., Celie, P.H.N., Brummelkamp, T.R., and Perrakis, A. (2019). Crystal structure of the tubulin tyrosine carboxypeptidase complex VASH1–SVBP. Nature Structural & Molecular Biology *26*, 567-570.

Aillaud, C., Bosc, C., Peris, L., Bosson, A., Heemeryck, P., Van Dijk, J., Le Friec, J., Boulan, B., Vossier, F., Sanman, L.E.*, et al.* (2017). Vasohibins/SVBP are tubulin carboxypeptidases (TCPs) that regulate neuron differentiation. Science *358*, 1448-1453.

Akera, T., Chmátal, L., Trimm, E., Yang, K., Aonbangkhen, C., Chenoweth, D.M., Janke, C., Schultz, R.M., and Lampson, M.A. (2017). Spindle asymmetry drives non-Mendelian chromosome segregation. Science *358*, 668-672.

Alieva, I.B., and Uzbekov, R.E. (2016). Where are the limits of the centrosome? BioArchitecture *6*, 47-52.

Arce, C.A., Rodriguez, J.A., Barra, H.S., and Caputto, R. (1975). Incorporation of l-Tyrosine, l-Phenylalanine and l-3,4-Dihydroxyphenylalanine as Single Units into Rat Brain Tubulin. European Journal of Biochemistry *59*, 145-149.

Audebert, S., Desbruyères, E., Gruszczynski, C., Koulakoff, A., Gros, F., Denoulet, P., and Eddé, B. (1993). Reversible polyglutamylation of alpha- and beta-tubulin and microtubule dynamics in mouse brain neurons. Molecular Biology of the Cell *4*, 615-626.

Ball, D.A., Mehta, G.D., Salomon-Kent, R., Mazza, D., Morisaki, T., Mueller, F., McNally, J.G., and Karpova, T.S. (2016). Single molecule tracking of Ace1p in Saccharomyces cerevisiae defines a characteristic residence time for non-specific interactions of transcription factors with chromatin. Nucleic Acids Research *44*, e160-e160.

Barisic, M., Silva E Sousa, R., Tripathy, S.K., Magiera, M.M., Zaytsev, A.V., Pereira, A.L., Janke, C., Grishchuk, E.L., and Maiato, H. (2015). Microtubule detyrosination guides chromosomes during mitosis. Science *348*, 799-803.

Barra, H.S., Rodriguez, J.A., Arce, C.A., and Caputto, R. (1973). A SOLUBLE PREPARATION FROM RAT BRAIN THAT INCORPORATES INTO ITS OWN PROTEINS [14C]ARGININE BY A RIBONUCLEASE-SENSITIVE SYSTEM AND [14C]TYROSINE BY A RIBONUCLEASE-INSENSITIVE SYSTEM. Journal of Neurochemistry *20*, 97-108.

Beese, L., Stubbs, G., and Cohen, C. (1987). Microtubule structure at 18 Å resolution. Journal of Molecular Biology *194*, 257-264.

Bénichou, O., Grebenkov, D.S., Levitz, P.E., Loverdo, C., and Voituriez, R. (2011). Mean First-Passage Time of Surface-Mediated Diffusion in Spherical Domains. Journal of Statistical Physics *142*, 657-685.

Bieling, P., Kandels-Lewis, S., Telley, I.A., Van Dijk, J., Janke, C., and Surrey, T. (2008). CLIP-170 tracks growing microtubule ends by dynamically recognizing composite EB1/tubulin-binding sites. Journal of Cell Biology *183*, 1223-1233.

Brackley, C.A., Cates, M.E., and Marenduzzo, D. (2013). Intracellular Facilitated Diffusion: Searchers, Crowders, and Blockers. Physical Review Letters *111*.

Bré, M.H., Kreis, T.E., and Karsenti, E. (1987). Control of microtubule nucleation and stability in Madin-Darby canine kidney cells: the occurrence of noncentrosomal, stable detyrosinated microtubules. Journal of Cell Biology *105*, 1283-1296.

Bressloff, P.C. (2020). Search processes with stochastic resetting and multiple targets. Physical Review E *102*.

Buttenschön, A., and Edelstein-Keshet, L. (2019). Correlated random walks inside a cell: actin branching and microtubule dynamics. Journal of Mathematical Biology *79*, 1953-1972.

Cassimeris, L., Leung, J.C., and Odde, D.J. (2018). Monte Carlo simulations of microtubule arrays: The critical roles of rescue transitions, the cell boundary, and tubulin concentration in shaping microtubule distributions. PLOS ONE *13*, e0197538.

Cella Zanacchi, F., Manzo, C., Magrassi, R., Derr, N.D., and Lakadamyali, M. (2019). Quantifying Protein Copy Number in Super Resolution Using an Imaging-Invariant Calibration. Biophysical Journal *116*, 2195-2203.

Chen, J., Kholina, E., Szyk, A., Fedorov, V.A., Kovalenko, I., Gudimchuk, N., and Roll-Mecak, A. (2021). α-tubulin tail modifications regulate microtubule stability through selective effector recruitment, not changes in intrinsic polymer dynamics. Developmental cell *56*, 2016-2028.e2014.

Chen, J., Zhang, Z., Li, L., Chen, B.-C., Revyakin, A., Hajj, B., Legant, W., Dahan, M., Lionnet, T., Betzig, E.*, et al.* (2014). Single-Molecule Dynamics of Enhanceosome Assembly in Embryonic Stem Cells. Cell *156*, 1274-1285.

Chevalier, C., Bénichou, O., Meyer, B., and Voituriez, R. (2010). First-passage quantities of Brownian motion in a bounded domain with multiple targets: a unified approach. Journal of Physics A: Mathematical and Theoretical *44*, 025002.

Dogterom, M., and Leibler, S. (1993). Physical aspects of the growth and regulation of microtubule structures. Physical Review Letters *70*, 1347-1350.

Ehmann, N., Van De Linde, S., Alon, A., Ljaschenko, D., Keung, X.Z., Holm, T., Rings, A., Diantonio, A., Hallermann, S., Ashery, U.*, et al.* (2014). Quantitative super-resolution imaging of Bruchpilot distinguishes active zone states. Nature Communications *5*.

Fredy, J.W., Méndez-Ardoy, A., Kwangmettatam, S., Bochicchio, D., Matt, B., Stuart, M.C.A., Huskens, J., Katsonis, N., Pavan, G.M., and Kudernac, T. (2017). Molecular photoswitches mediating the strain-driven disassembly of supramolecular tubules. Proceedings of the National Academy of Sciences *114*, 11850-11855.

Gómez-García, P.A., Portillo-Ledesma, S., Neguembor, M.V., Pesaresi, M., Oweis, W., Rohrlich, T., Wieser, S., Meshorer, E., Schlick, T., Cosma, M.P.*, et al.* (2021). Mesoscale Modeling and Single-Nucleosome Tracking Reveal Remodeling of Clutch Folding and Dynamics in Stem Cell Differentiation. Cell Reports *34*, 108614.

Grignard, J., Lamamy, V., Vermersch, E., Delagrange, P., Stephan, J.-P., Dorval, T., and Fages, F. (2022). Mathematical modeling of the microtubule detyrosination/tyrosination cycle for cell-based drug screening design. PLOS Computational Biology *18*, e1010236.

Grimm, J.B., English, B.P., Chen, J., Slaughter, J.P., Zhang, Z., Revyakin, A., Patel, R., Macklin, J.J., Normanno, D., Singer, R.H.*, et al.* (2015). A general method to improve fluorophores for live-cell and single-molecule microscopy. Nature Methods *12*, 244-250.

Gundersen, G.G., and Bulinski, J.C. (1986). Distribution of tyrosinated and nontyrosinated alpha-tubulin during mitosis. Journal of Cell Biology *102*, 1118-1126.

Gundersen, G.G., Khawaja, S., and Bulinski, J.C. (1987). Postpolymerization detyrosination of alpha-tubulin: a mechanism for subcellular differentiation of microtubules. Journal of Cell Biology *105*, 251-264.

Gyparaki, M.T., Arab, A., Sorokina, E.M., Santiago-Ruiz, A.N., Bohrer, C.H., Xiao, J., and Lakadamyali, M. (2021). Tau forms oligomeric complexes on microtubules that are distinct from tau aggregates. Proceedings of the National Academy of Sciences *118*, e2021461118.

Izeddin, I., Récamier, V., Bosanac, L., Cissé, I.I., Boudarene, L., Dugast-Darzacq, C., Proux, F., Bénichou, O., Voituriez, R., Bensaude, O.*, et al.* (2014). Single-molecule tracking in live cells reveals distinct target-search strategies of transcription factors in the nucleus. eLife *3*.

Janke, C., and Magiera, M.M. (2020). The tubulin code and its role in controlling microtubule properties and functions. Nature Reviews Molecular Cell Biology.

Jeffrey, Maria, Jacob, Janke, C., and Erika (2016). α-Tubulin Tyrosination and CLIP-170 Phosphorylation Regulate the Initiation of Dynein-Driven Transport in Neurons. Cell Reports *14*, 2637-2652.

Jiang, K., Hua, S., Mohan, R., Grigoriev, I., Kah, Liu, Q., Eugene, A.F, Albert, Casper*, et al.* (2014). Microtubule Minus-End Stabilization by Polymerization-Driven CAMSAP Deposition. Developmental cell *28*, 295-309.

Jungmann, R., Avendano, M.S., Woehrstein, J.B., Dai, M., Shih, W.M., and Yin, P. (2014). Multiplexed 3D cellular super-resolution imaging with DNA-PAINT and Exchange-PAINT. Nat Methods *11*, 313-318.

Katrukha, E.A., Jurriens, D., Salas Pastene, D.M., and Kapitein, L.C. (2021). Quantitative mapping of dense microtubule arrays in mammalian neurons. eLife *10*.

Kesarwani, S., Lama, P., Chandra, A., Reddy, P.P., Jijumon, A.S., Bodakuntla, S., Rao, B.M., Janke, C., Das, R., and Sirajuddin, M. (2020). Genetically encoded live-cell sensor for tyrosinated microtubules. Journal of Cell Biology *219*.

Khawaja, S., Gundersen, G.G., and Bulinski, J.C. (1988). Enhanced stability of microtubules enriched in detyrosinated tubulin is not a direct function of detyrosination level. Journal of Cell Biology *106*, 141-149.

Konishi, Y., and Setou, M. (2009). Tubulin tyrosination navigates the kinesin-1 motor domain to axons. Nature Neuroscience *12*, 559-567.

Kreis, T.E. (1987). Microtubules containing detyrosinated tubulin are less dynamic. The EMBO Journal *6*, 2597-2606.

Lacroix, B., Van Dijk, J., Gold, N.D., Guizetti, J., Aldrian-Herrada, G., Rogowski, K., Gerlich, D.W., and Janke, C. (2010). Tubulin polyglutamylation stimulates spastin-mediated microtubule severing. Journal of Cell Biology *189*, 945-954.

Landskron, L., Bak, J., Adamopoulos, A., Kaplani, K., Moraiti, M., Hengel, L.G.v.d., Song, J.-Y., Bleijerveld, O.B., Nieuwenhuis, J., Heidebrecht, T.*, et al.* (2022). Posttranslational modification of microtubules by the MATCAP detyrosinase. Science *376*, eabn6020.

Ledbetter, M.C., and Porter, K.R. (1963). A "MICROTUBULE" IN PLANT CELL FINE STRUCTURE. Journal of Cell Biology *19*, 239-250.

Li, F., Hu, Y., Qi, S., Luo, X., and Yu, H. (2019). Structural basis of tubulin detyrosination by vasohibins. Nature Structural & Molecular Biology *26*, 583-591.

Li, F., Li, Y., Ye, X., Gao, H., Shi, Z., Luo, X., Rice, L.M., and Yu, H. (2020). Cryo-EM structure of VASH1-SVBP bound to microtubules. eLife *9*.

Liao, S., Rajendraprasad, G., Wang, N., Eibes, S., Gao, J., Yu, H., Wu, G., Tu, X., Huang, H., Barisic, M.*, et al.* (2019). Molecular basis of vasohibins-mediated detyrosination and its impact on spindle function and mitosis. Cell Research *29*, 533-547.

Ly, N., Elkhatib, N., Bresteau, E., Piétrement, O., Khaled, M., Magiera, M.M., Janke, C., Le Cam, E., Rutenberg, A.D., and Montagnac, G. (2016). αTAT1 controls longitudinal spreading of acetylation marks from open microtubules extremities. Scientific Reports *6*, 35624.

Mazza, D., Abernathy, A., Golob, N., Morisaki, T., and McNally, J.G. (2012). A benchmark for chromatin binding measurements in live cells. Nucleic Acids Research *40*, e119-e119.

McKenney, R.J., Huynh, W., Vale, R.D., and Sirajuddin, M. (2016). Tyrosination of α-tubulin controls the initiation of processive dynein–dynactin motility. The EMBO Journal *35*, 1175-1185.

Mirny, L., Slutsky, M., Wunderlich, Z., Tafvizi, A., Leith, J., and Kosmrlj, A. (2009). How a protein searches for its site on DNA: the mechanism of facilitated diffusion. Journal of Physics A: Mathematical and Theoretical *42*, 434013.

Mohan, N., Sorokina, E.M., Verdeny, I.V., Alvarez, A.S., and Lakadamyali, M. (2019). Detyrosinated microtubules spatially constrain lysosomes facilitating lysosome–autophagosome fusion. Journal of Cell Biology *218*, 632-643.

Mutothya, N.M., and Xu, Y. (2021). Mean first passage time for diffuse and rest search in a confined spherical domain. Physica A: Statistical Mechanics and its Applications *567*, 125667.

Nieuwenhuis, J., Adamopoulos, A., Bleijerveld, O.B., Mazouzi, A., Stickel, E., Celie, P., Altelaar, M., Knipscheer, P., Perrakis, A., Blomen, V.A.*, et al.* (2017). Vasohibins encode tubulin detyrosinating activity. Science *358*, 1453-1456.

Normanno, D., Boudarène, L., Dugast-Darzacq, C., Chen, J., Richter, C., Proux, F., Bénichou, O., Voituriez, R., Darzacq, X., and Dahan, M. (2015). Probing the target search of DNA-binding proteins in mammalian cells using TetR as model searcher. Nature Communications *6*, 7357.

Peris, L., Thery, M., Fauré, J., Saoudi, Y., LafanechèRe, L., Chilton, J.K., Gordon-Weeks, P., Galjart, N., Bornens, M., Wordeman, L.*, et al.* (2006). Tubulin tyrosination is a major factor affecting the recruitment of CAP-Gly proteins at microtubule plus ends. Journal of Cell Biology *174*, 839-849.

Peris, L., Wagenbach, M., Lafanechère, L., Brocard, J., Moore, A.T., Kozielski, F., Job, D., Wordeman, L., and Andrieux, A. (2009). Motor-dependent microtubule disassembly driven by tubulin tyrosination. Journal of Cell Biology *185*, 1159-1166.

Pordes, R., Petravick, D., Kramer, B., Olson, D., Livny, M., Roy, A., Avery, P., Blackburn, K., Wenaus, T., Würthwein, F.*, et al.* (2007). The open science grid. Journal of Physics: Conference Series *78*, 012057.

Raybin, D., and Flavin, M. (1975). An enzyme tyrosylating α-tubulin and its role in microtubule assembly. Biochemical and Biophysical Research Communications *65*, 1088-1095.

Robison, P., Caporizzo, M.A., Ahmadzadeh, H., Bogush, A.I., Chen, C.Y., Margulies, K.B., Shenoy, V.B., and Prosser, B.L. (2016). Detyrosinated microtubules buckle and bear load in contracting cardiomyocytes. Science *352*, aaf0659.

Roll-Mecak, A. (2019). How cells exploit tubulin diversity to build functional cellular microtubule mosaics. Current Opinion in Cell Biology *56*, 102-108.

Schatten, H. (2008). The mammalian centrosome and its functional significance. Histochemistry and Cell Biology *129*, 667-686.

Schöneberg, J., Ullrich, A., and Noé, F. (2014). Simulation tools for particle-based reaction-diffusion dynamics in continuous space. BMC Biophysics *7*.

Schulze, E., and Kirschner, M. (1987). Dynamic and stable populations of microtubules in cells. Journal of Cell Biology *104*, 277-288.

Sensale, S., Sharma, P., and Arya, G. (2022). Binding kinetics of harmonically confined random walkers. Physical Review E *105*, 044136.

Sfiligoi, I., Bradley, D.C., Holzman, B., Mhashilkar, P., Padhi, S., and Wurthwein, F. (2009). The Pilot Way to Grid Resources Using glideinWMS. Paper presented at: 2009 WRI World Congress on Computer Science and Information Engineering.

Shelden, E., and Wadsworth, P. (1993). Observation and quantification of individual microtubule behavior in vivo: microtubule dynamics are cell-type specific. Journal of Cell Biology *120*, 935-945.

Shin, S.C., Im, S.-K., Jang, E.-H., Jin, K.S., Hur, E.-M., and Kim, E.E. (2019). Structural and Molecular Basis for Katanin-Mediated Severing of Glutamylated Microtubules. Cell Reports *26*, 1357-1367.e1355.

Sirajuddin, M., Rice, L.M., and Vale, R.D. (2014). Regulation of microtubule motors by tubulin isotypes and post-translational modifications. Nature cell biology *16*, 335-344.

Slutsky, M., and Mirny, L.A. (2004). Kinetics of Protein-DNA Interaction: Facilitated Target Location in Sequence-Dependent Potential. Biophysical Journal *87*, 4021-4035.

Spichal, M., and Fabre, E. (2017). The Emerging Role of the Cytoskeleton in Chromosome Dynamics. Front Genet *8*, 60.

Steinmetz, M.O., and Akhmanova, A. (2008). Capturing protein tails by CAP-Gly domains. Trends in Biochemical Sciences *33*, 535-545.

Suzuki, Y., Kobayashi, M., Miyashita, H., Ohta, H., Sonoda, H., and Sato, Y. (2010). Isolation of a small vasohibin-binding protein (SVBP) and its role in vasohibin secretion. *123*, 3094-3101.

Szyk, A., Deaconescu, A.M., Piszczek, G., and Roll-Mecak, A. (2011). Tubulin tyrosine ligase structure reveals adaptation of an ancient fold to bind and modify tubulin. Nature Structural & Molecular Biology *18*, 1250-1258.

Tas, R.P., Chazeau, A., Cloin, B.M.C., Lambers, M.L.A., Hoogenraad, C.C., and Kapitein, L.C. (2017). Differentiation between Oppositely Oriented Microtubules Controls Polarized Neuronal Transport. Neuron *96*, 1264-1271.e1265.

Tinevez, J.-Y., Perry, N., Schindelin, J., Hoopes, G.M., Reynolds, G.D., Laplantine, E., Bednarek, S.Y., Shorte, S.L., and Eliceiri, K.W. (2017). TrackMate: An open and extensible platform for single-particle tracking. Methods *115*, 80-90.

Tokunaga, M., Imamoto, N., and Sakata-Sogawa, K. (2008). Highly inclined thin illumination enables clear single-molecule imaging in cells. Nature Methods *5*, 159-161.

Ullrich, A., Böhme, M.A., Schöneberg, J., Depner, H., Sigrist, S.J., and Noé, F. (2015). Dynamical Organization of Syntaxin-1A at the Presynaptic Active Zone. PLOS Computational Biology *11*, e1004407.

Valenstein, Max L., and Roll-Mecak, A. (2016). Graded Control of Microtubule Severing by Tubulin Glutamylation. Cell *164*, 911-921.

Wang, N., Bosc, C., Ryul Choi, S., Boulan, B., Peris, L., Olieric, N., Bao, H., Krichen, F., Chen, L., Andrieux, A.*, et al.* (2019). Structural basis of tubulin detyrosination by the vasohibin–SVBP enzyme complex. Nature Structural & Molecular Biology *26*, 571-582.

Webster, D.R. (1990). Detyrosination of alpha tubulin does not stabilize microtubules in vivo [published erratum appears in J Cell Biol 1990 Sep;111(3):1325-6]. The Journal of Cell Biology *111*, 113-122.

Webster, D.R., Gundersen, G.G., Bulinski, J.C., and Borisy, G.G. (1987a). Assembly and turnover of detyrosinated tubulin in vivo. Journal of Cell Biology *105*, 265-276.

Webster, D.R., Gundersen, G.G., Bulinski, J.C., and Borisy, G.G. (1987b). Differential turnover of tyrosinated and detyrosinated microtubules. Proceedings of the National Academy of Sciences *84*, 9040-9044.

Weisbrich, A., Honnappa, S., Jaussi, R., Okhrimenko, O., Frey, D., Jelesarov, I., Akhmanova, A., and Steinmetz, M.O. (2007). Structure-function relationship of CAP-Gly domains. Nature Structural & Molecular Biology *14*, 959-967.

Yu, X., Chen, X., Amrute-Nayak, M., Allgeyer, E., Zhao, A., Chenoweth, H., Clement, M., Harrison, J., Doreth, C., Sirinakis, G.*, et al.* (2021). MARK4 controls ischaemic heart failure through microtubule detyrosination. Nature *594*, 560-565.

Zanacchi, F.C., Manzo, C., Alvarez, A.S., Derr, N.D., Garcia-Parajo, M.F., and Lakadamyali, M. (2017). A DNA origami platform for quantifying protein copy number in super-resolution. Nature Methods *14*, 789-792.

Zhan, P., Jahnke, K., Liu, N., and Göpfrich, K. (2022). Functional DNA-based cytoskeletons for synthetic cells. Nature Chemistry.

Zhou, C., Yan, L., Zhang, W.-H., and Liu, Z. (2019). Structural basis of tubulin detyrosination by VASH2/SVBP heterodimer. Nature Communications *10*.